A dynamic elastoplastic model of concrete based on a modeling method with environmental factors as constitutive variables

Dechun Lu [1], Fanping Meng [2], Xin Zhou [3], Yuhang Zhuo [4], Zhiwei Gao [5], Xiuli Du [6]

[1]Professor, Key Laboratory of Urban Security and Disaster Engineering of Ministry of Education, Beijing University of Technology, Beijing 100124, China. E-mail: dechun@bjut.edu.cn

[2]Ph.D. Candidate, Key Laboratory of Urban Security and Disaster Engineering of Ministry of Education, Beijing University of Technology, Beijing 100124, China. E-mail: mengfp@emails.bjut.edu.cn

[*3]Research assistant, Key Laboratory of Urban Security and Disaster Engineering of Ministry of Education, Beijing University of Technology, Beijing 100124, China; Key Laboratory of Civil Engineering Safety and Durability of China Education Ministry, Tsinghua University, Beijing 100084, China. E-mail: zhouxin615@tsinghua.edu.cn

[4]Master's Candidate, Key Laboratory of Urban Security and Disaster Engineering of Ministry of Education, Beijing University of Technology, Beijing 100124, China. E-mail: zhuoyuhang@emails.bjut.edu.cn

[5]Senior Lecturer, James Watt School of Engineering, University of Glasgow, Glasgow, G12 8QQ, UK. E-mail: zhiwei.gao@glasgow.ac.uk

[6]Professor, Key Laboratory of Urban Security and Disaster Engineering of Ministry of Education, Beijing University of Technology, Beijing 100124, China. E-mail: duxiuli@bjut.edu.cn

Corresponding author

Xin Zhou, Key Laboratory of Urban Security and Disaster Engineering of Ministry of Education, Beijing University of Technology, Beijing 100124, China; Key Laboratory of Civil Engineering Safety and Durability of China Education Ministry, Tsinghua University, Beijing 100084, China. E-mail: zhouxin615@tsinghua.edu.cn

Abstract

This paper develops a modeling method with incremental stress–strain–environment constitutive model to predict the change in the plastic mechanical behavior of concrete caused by environmental action, and it regards the environmental factor as a constitutive variable, similar to stress and strain. The yield condition of the model is a function of stress, the plastic internal variable, and the environmental variable. The loading–unloading criterion is established in the space constructed by the strain and the environmental variable to determine the contribution of mechanical loads and environmental factors to plastic deformation. By considering the strain rate as an environmental factor and applying the proposed method, a stress–strain–strain rate constitutive model of concrete is developed to describe the plastic flow caused by the combined action of stress and strain rate. In addition, constant- and variable-strain rate loading tests are performed to evaluate the performance of the established model. In particular, the model's capabilities are further highlighted by comparing the simulation results of the dynamic stress–strain model and the proposed model under loading conditions with rapidly decreasing strain rates.

Keywords: Concrete; Constitutive model; Environment; Dynamic; Tests

Introduction

The classical elastoplastic constitutive model of concrete is devoted to establishing the stress–strain relationship in a constant environmental state, i.e., $\mathrm{d}\boldsymbol{\sigma} = \mathbf{D} : \mathrm{d}\boldsymbol{\varepsilon}$, in which the material parameters in the stiffness matrix $(\mathbf{D})$ are independent of the external environment. However, extreme weather and events make concrete structures face the threat of drastic environmental changes during real services (Jia et al., 2023; Wehner et al., 2021). Experimental results show that the material parameters of concrete are susceptible to specific environments (Wu et al., 2015). For example, the uniaxial tensile/compressive strengths enlarge with increasing strain rate (Kong et al., 2018; Shkolnik, 2008; Zeng et al., 2023) but decrease with raising temperature (Chang et al., 2006; Chen et al., 2015; He et al., 2021), where strain rate and temperature are two typical environmental variables. Environmental variables (ψ) are used to represent environmental factors that affect the material parameters of concrete. It is imperative to develop corresponding constitutive models to capture the mechanical response of concrete in a variable environmental state (Fan et al., 2022; Gasch et al., 2016).

Taking dynamic loads as an environmental factor, there are generally two methods of establishing constitutive relations to reflect the mechanical characteristics affected by the environment. One simplified method is to introduce ψ into the material parameters in the stiffness matrix, i.e., $\mathrm{d}\boldsymbol{\sigma} = \mathbf{D}(\psi) : \mathrm{d}\boldsymbol{\varepsilon}$. The constitutive relation established at this time is still of the incremental stress–strain form (Gao and Zhao, 2017; Kong et al., 2017). Several popular concrete models, e.g., the Holmquist–Johnson–Cook model (Holmquist and Johnson, 2011), the Riedel–Hiermaier–Thoma model (Borrvall and Riedel, 2011), and the Karagozian and Case model (Kong et al., 2017), have been developed based on this modeling method. Their common feature is that the strength parameter in the yield function is strain-rate-dependent (Malvar et al., 1997; Polanco-Loria et al., 2008), and the environmental sensitivity of material parameters can be reasonably considered. However, when performing the consistency condition in the differential form to determine the plasticity multiplier, it is assumed that the strain rate is constant (Bai et al., 2020). Here, the strain rate, an environmental variable, is considered a factor influencing material parameters rather than a constitutive variable. The advantage of this method is that the existing damage model or plastic model can be directly developed into a model considering the environmental influence by developing model parameters into functions of environmental factors, but the mechanical response caused by the environmental change cannot be captured.

Another method is to treat environmental factors as constitutive variables similar to stress and strain, i.e., $\mathrm{d}\boldsymbol{\sigma} = \mathbf{D}(\psi) : \mathrm{d}\boldsymbol{\varepsilon} + \mathbf{D}_{\psi}\mathrm{d}\psi$. The constitutive model is established in the form of incremental stress–strain–environment to describe the mechanical response of concrete under the coupled action of load and environment (Lu et al., 2020). Especially, the mechanical response, i.e., $\mathbf{D}_{\psi}\mathrm{d}\psi$, caused by the changes in the environment can be captured (Hossain and Weiss, 2004; Rahnavard et al., 2022; Torelli et al., 2018). The viscoplastic model is a representative model established by this method. Here, the viscoplastic strain rate is considered as a constitutive variable in calculating the viscoplastic multiplier (Aráoz and Luccioni, 2015; Kang and Willam, 2000), so the relaxation or creep process caused by a change in viscoplastic strain rate can be described (Naghdi and Murch, 1963). However, neglecting the elastic strain rate prevents the relaxation process (creep process) of the stress state beginning within the yield surface from being captured (Heeres et al., 2002; Qiao et al., 2016). There are few reports on establishing the incremental stress–strain–environment constitutive model by introducing the total strain rate into the yield function. In this context, Lu et al. (2020) establish a dynamic constitutive model for concrete regarding the total strain rate as a constitutive variable in the yield function. The yield function was taken into account as a function of plastic internal variables, stress, total strain rate, and temperature in Ma et al.'s (2022) dynamic thermal, elastoplastic damage model. The plastic deformation caused by changes in strain rate and temperature could be described since environmental factors were considered constitutive variables.

Therefore, it can be inferred that introducing environmental factors into the yield function as constitutive variables is a tremendous approach to developing the incremental stress–strain–environment constitutive models. However, a complete modeling method also needs a loading–unloading criterion for judging when concrete produces plastic strain in addition to incremental stress–strain–environment relationship. The classical loading–unloading criteria based on Drucker's postulate in the stress space (Drucker, 1950) or Ilyushin's postulate in the strain space (Il'Iushin, 1961) only applies to the incremental stress–strain constitutive relation. For the incremental stress–strain–environment constitutive relation, the environmental variable can also change the stress or strain state of the concrete. Hence, a combined coordinate space, namely the stress and the environmental factor or the strain and the environmental factor, should be chosen to develop the corresponding loading–unloading criterion, which is eagerly needed for perfecting the modeling method of incremental stress–strain–environment form in plastic theory.

To this end, next section presents an approach for establishing incremental relationships between constitutive variables, i.e., the stress, strain, and environmental factors, and the corresponding loading–unloading criterion is proposed under the combined action of environmental factors and mechanical loads. The constitutive model of concrete with incremental stress–strain–strain rate form is developed with strain rate as an environmental variable. Next, experiments with constant- and variable-strain rates are performed to investigate the dynamic mechanical behavior of concrete. Model predictions are contrasted with experimental findings, and the performance of the proposed model is deeply studied. Section "Conclusions" summarizes the work of this paper.

Modeling method in the incremental stress–strain–environment form

A complete modeling method of a constitutive relation with incremental stress–strain–environment form requires solving two problems: (*i*) How can environmental factors be introduced into the incremental stress–strain relationship and further developed into the incremental stress–strain–environment relationship? (*ii*) What are the conditions for the occurrence of a plastic strain, i.e., the loading–unloading criterion, under the combined action of mechanical loads and environmental factors? This section presents the solutions to these two problems based on the small strain assumption.

Incremental stress–strain–environment relation

In the theory of plasticity, the yield function is a mathematical description of the material mechanical state when a plastic flow occurs, which distinguishes the boundary between elastic and plastic deformation. When environmental factors remain unchanged, the yield function is a function of the stress and hardening parameter:

$$f\left[\boldsymbol{\sigma}, H(\boldsymbol{\varepsilon}^{\mathrm{p}})\right] = 0 \tag{1}$$

where $\boldsymbol{\sigma}$ is the stress tensor. $\boldsymbol{\varepsilon}^{\mathrm{p}}$ represents the plastic strain tensor. H indicates the hardening parameter that records the loading history of the material. The accumulation of plastic strain will lead to an increase of H. Further, for the hardening material, the yield surface also extends outward correspondingly, which indicates that the elastic range of the material is enlarged. When environmental factors change, the yield function is not only a function of both $\boldsymbol{\sigma}$ and H but also of environmental factors (ψ):

$$f\left[\boldsymbol{\sigma}, \psi, H(\boldsymbol{\varepsilon}^{\mathrm{p}})\right] = 0 \tag{2}$$

where ψ is introduced into the yield function as a constitutive variable similar to $\boldsymbol{\sigma}$. In other words, a combined coordinate space consisting of the stress dimension and the environmental variable dimension is required to completely present the yield function defined by Eq. (2). When plastic strain occurs, the state point including stress and environmental factors must be on the yield surface, which is also called the consistency condition. Taking the full derivative of Eq. (2), one can obtain the consistency condition in a differential form as follows:

$$\mathrm{d}f = \frac{\partial f}{\partial \boldsymbol{\sigma}} : \mathrm{d}\boldsymbol{\sigma} + \frac{\partial f}{\partial \psi}\mathrm{d}\psi + \frac{\partial f}{\partial H}\frac{\partial H}{\partial \boldsymbol{\varepsilon}^{\mathrm{p}}} : \mathrm{d}\boldsymbol{\varepsilon}^{\mathrm{p}} = 0 \tag{3}$$

where $\left(\partial f / \partial \psi\right)\mathrm{d}\psi$ considers the contribution of the change in the environmental variable to the plastic strain. For a given strain increment ($\mathrm{d}\boldsymbol{\varepsilon}$) and an environmental variable increment ($\mathrm{d}\psi$), Eq. (3) has two unknowns: stress increment ($\mathrm{d}\boldsymbol{\sigma}$) and plastic strain increment ($\mathrm{d}\boldsymbol{\varepsilon}^{\mathrm{p}}$). According to the flow rule and Hooke's law, following equations can be obtained:

$$\mathrm{d}\boldsymbol{\varepsilon}^{\mathrm{p}} = \mathrm{d}\Lambda \cdot \mathbf{r} \tag{4}$$

$$\mathrm{d}\boldsymbol{\sigma} = \mathbf{D}^{\mathrm{e}} : \mathrm{d}\boldsymbol{\varepsilon}^{\mathrm{e}} = \mathbf{D}^{\mathrm{e}} : \left(\mathrm{d}\boldsymbol{\varepsilon} - \mathrm{d}\boldsymbol{\varepsilon}^{\mathrm{p}}\right) \tag{5}$$

where $\mathrm{d}\Lambda$ and $\mathbf{r}$ denote the magnitude and direction of $\mathrm{d}\boldsymbol{\varepsilon}^{\mathrm{p}}$ respectively. $\mathbf{r}$ can be determined by the orthogonal flow rule (Paliwal et al., 2020; Zheng and Teng, 2022) or the non-orthogonal flow rule (Lu et al., 2022; Lu et al., 2019). The former uses the orthogonal gradient of the constructed plastic potential function to determine $\mathbf{r}$. The latter directly determines $\mathbf{r}$ by obtaining the non-orthogonal gradient of the yield function. $\mathbf{D}^{\mathrm{e}}$ indicates the elastic stiffness tensor. $\mathrm{d}\boldsymbol{\varepsilon}^{\mathrm{e}}$ is the elastic strain increment.

Eq. (5) describes the incremental stress–strain relationship under elastic loading. Invoking Eqs. (4) and (5) into Eq. (3) defines $\mathrm{d}\Lambda$ as:

$$\mathrm{d}\Lambda = \frac{\dfrac{\partial f}{\partial \boldsymbol{\sigma}} : \mathbf{D}^{\mathrm{e}} : \mathrm{d}\boldsymbol{\varepsilon}}{\dfrac{\partial f}{\partial \boldsymbol{\sigma}} : \mathbf{D}^{\mathrm{e}} : \mathbf{r} - \dfrac{\partial f}{\partial H}\dfrac{\partial H}{\partial \boldsymbol{\varepsilon}^{\mathrm{p}}} : \mathbf{r}} + \frac{\dfrac{\partial f}{\partial \psi}\mathrm{d}\psi}{\dfrac{\partial f}{\partial \boldsymbol{\sigma}} : \mathbf{D}^{\mathrm{e}} : \mathbf{r} - \dfrac{\partial f}{\partial H}\dfrac{\partial H}{\partial \boldsymbol{\varepsilon}^{\mathrm{p}}} : \mathbf{r}} \tag{6}$$

Combining Eqs. (4)–(6) can obtain the incremental stress–strain–environment constitutive relation during the plastic loading as follows:

$$\mathrm{d}\boldsymbol{\sigma} = \left[\mathbf{D}^{\mathrm{e}} - \frac{\left(\mathbf{D}^{\mathrm{e}} : \mathbf{r}\right) \otimes \dfrac{\partial f}{\partial \boldsymbol{\sigma}} : \mathbf{D}^{\mathrm{e}}}{\dfrac{\partial f}{\partial \boldsymbol{\sigma}} : \mathbf{D}^{\mathrm{e}} : \mathbf{r} - \dfrac{\partial f}{\partial H}\dfrac{\partial H}{\partial \boldsymbol{\varepsilon}^{\mathrm{p}}} : \mathbf{r}}\right] : \mathrm{d}\boldsymbol{\varepsilon} - \frac{\left(\mathbf{D}^{\mathrm{e}} : \mathbf{r}\right) \otimes \dfrac{\partial f}{\partial \psi}}{\dfrac{\partial f}{\partial \boldsymbol{\sigma}} : \mathbf{D}^{\mathrm{e}} : \mathbf{r} - \dfrac{\partial f}{\partial H}\dfrac{\partial H}{\partial \boldsymbol{\varepsilon}^{\mathrm{p}}} : \mathbf{r}}\mathrm{d}\psi \tag{7}$$

Eq. (7) can describe the mechanical response caused by environmental changes. In particular, the incremental stress–strain–environment relationship degenerates into the incremental stress–strain relationship when the environmental variable is constant, i.e., $\mathrm{d}\psi = 0$.

Loading–unloading criterion under combined action of strain and environment

The loading–unloading criterion evaluates whether the plastic flow occurs in the material according to the geometric relationship between the load vector and the yield surface at the current state point. The load vector comprises the stress increment and the environmental variable increment. Therefore, the stress–environmental variable coordinate space is required to fully represent the geometric relationship between the load vector and the yield surface, as shown in Fig. 1.

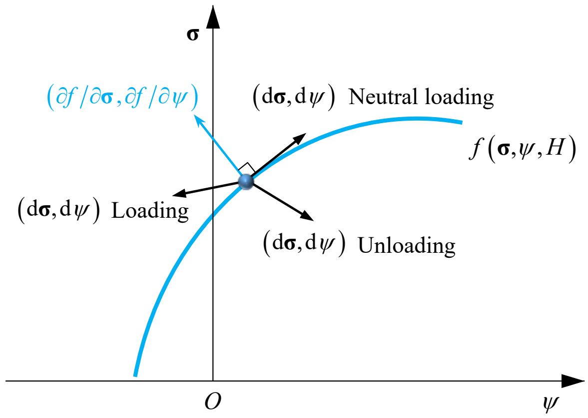

Fig. 1. Loading–unloading criterion under the stress–environmental variable coordinate space.

Here, the changes in both the stress and the environmental variable determine the loading–unloading states under the current increment step. When the included angle between the load vector $\left(\mathrm{d}\boldsymbol{\sigma},\mathrm{d}\psi\right)$ and the yield surface's external normal direction $(\partial f/\partial\boldsymbol{\sigma},\partial f/\partial\psi)$ is acute, the material is in a loaded state. When the included angle is a right angle or obtuse angle, the material is in neutral loading (Lucchesi and Podio-Guidugli, 1995) or unloaded state respectively. Eq. (8) can be used to articulate Fig. 1.

$$\left(\frac{\partial f}{\partial\boldsymbol{\sigma}},\frac{\partial f}{\partial\psi}\right)\cdot\left(\mathrm{d}\boldsymbol{\sigma},\mathrm{d}\psi\right)=\begin{cases}\dfrac{\partial f}{\partial\boldsymbol{\sigma}}:\mathrm{d}\boldsymbol{\sigma}+\dfrac{\partial f}{\partial\psi}\mathrm{d}\psi>0 & \text{Loading}\\ \dfrac{\partial f}{\partial\boldsymbol{\sigma}}:\mathrm{d}\boldsymbol{\sigma}+\dfrac{\partial f}{\partial\psi}\mathrm{d}\psi=0 & \text{Neutral loading}\\ \dfrac{\partial f}{\partial\boldsymbol{\sigma}}:\mathrm{d}\boldsymbol{\sigma}+\dfrac{\partial f}{\partial\psi}\mathrm{d}\psi<0 & \text{Unloading}\end{cases} \tag{8}$$

Eq. (8) based on Drucker's postulate applies only to hardened materials. For concrete with softening properties, the loading–unloading criterion needs to be transformed into the form of the strain–environmental variable according to Ilyushin's postulate (Il'lushin, 1961):

$$
\frac{\partial F}{\partial \boldsymbol{\varepsilon}}:\mathrm{d}\boldsymbol{\varepsilon}+\frac{\partial F}{\partial \psi}\mathrm{d}\psi=\begin{cases}\dfrac{\partial f}{\partial \boldsymbol{\sigma}}:\mathbf{D}^{\mathrm{e}}:\mathrm{d}\boldsymbol{\varepsilon}+\dfrac{\partial f}{\partial \psi}\mathrm{d}\psi>0 & \text{Loading}\\ \dfrac{\partial f}{\partial \boldsymbol{\sigma}}:\mathbf{D}^{\mathrm{e}}:\mathrm{d}\boldsymbol{\varepsilon}+\dfrac{\partial f}{\partial \psi}\mathrm{d}\psi=0 & \text{Neutral loading}\\ \dfrac{\partial f}{\partial \boldsymbol{\sigma}}:\mathbf{D}^{\mathrm{e}}:\mathrm{d}\boldsymbol{\varepsilon}+\dfrac{\partial f}{\partial \psi}\mathrm{d}\psi<0 & \text{Unloading}\end{cases} \tag{9}
$$

where F represents the yield function expressed by the strain and environmental variable, i.e., $F(\boldsymbol{\varepsilon},\psi,H)=f(\boldsymbol{\sigma},\psi,H)$. The transition between $\partial F/\partial\boldsymbol{\varepsilon}$ and $\partial f/\partial\boldsymbol{\sigma}$ can be obtained by the chain rule (Lu et al., 2020). The new loading-unloading criterion defined by Eq. (9) shows that the contribution of the variation in the environmental variable to plastic deformation can be considered. When the environment in which the material is located does not change, i.e., $\mathrm{d}\psi=0$, the deformation behavior of the material under the current load increment is estimated by the yield surface in the strain space (see Fig. 2). The plastic flow occurs only under the action of mechanical loads, i.e., $\partial F/\partial\boldsymbol{\varepsilon}:\mathrm{d}\boldsymbol{\varepsilon}>0$, as expressed in Eq. (10).

$$
\frac{\partial F}{\partial \boldsymbol{\varepsilon}}:\mathrm{d}\boldsymbol{\varepsilon}=\begin{cases}\dfrac{\partial f}{\partial \boldsymbol{\sigma}}:\mathbf{D}^{\mathrm{e}}:\mathrm{d}\boldsymbol{\varepsilon}>0 & \text{Loading}\\ \dfrac{\partial f}{\partial \boldsymbol{\sigma}}:\mathbf{D}^{\mathrm{e}}:\mathrm{d}\boldsymbol{\varepsilon}=0 & \text{Neutral loading}\\ \dfrac{\partial f}{\partial \boldsymbol{\sigma}}:\mathbf{D}^{\mathrm{e}}:\mathrm{d}\boldsymbol{\varepsilon}<0 & \text{Unloading}\end{cases} \tag{10}
$$

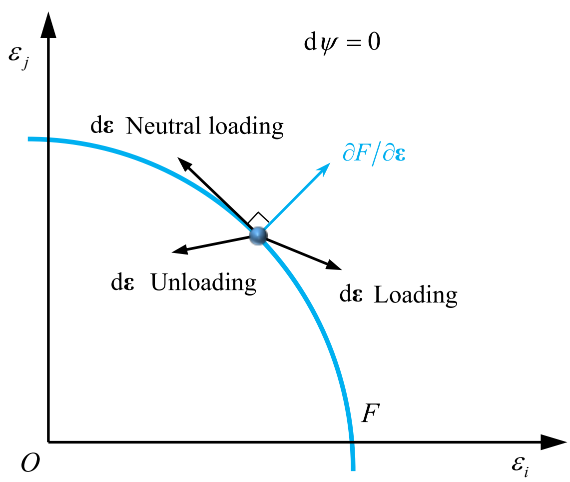

Fig. 2. Loading–unloading criterion for a constant environmental variable.

Based on the above analysis, solutions to two problems are given. Firstly, incremental stress–strain is developed as a stress–strain–environment relation by introducing environmental factor as a constitutive variable into the yield function. Secondly, the loading–unloading criterion is established in the combined space of strain and environment variable based on Ilyushin's postulate. So far, a complete modeling method for the incremental stress-strain-environment relationship is presented.

Constitutive model of incremental stress–strain–strain rate form of concrete

The strength of concrete significantly increases as the strain rate increases (Li et al., 2009; Peng et al., 2023). Based on the modeling method with incremental stress–strain–environment relation proposed in Section "Modeling Method in the Incremental Stress–Strain–Environment Form", the relation with incremental stress–strain–strain rate form is developed, and the corresponding loading–unloading criterion is established in the combined coordinate space of strain–strain rate.

Incremental stress–strain–strain rate relation

A general expression of incremental stress–strain–environment relation is given in Eq. (7). According to Eq. (7), to establish a model with strain rate as a constitutive variable, the expressions for yield function, hardening parameter, and flow rule need to be provided, in which strain rate is introduced into strength parameters. The yield function, hardening parameter, and consistency criterion are combined to determine $\mathrm{d}\Lambda$. The flow rule is used to calculate $\mathbf{r}$.

Yield function

The advantage of the closed yield function is that it can simultaneously represent the plastic deformation behavior of concrete under shear load and hydrostatic pressure load. A dynamic closed yield function is developed by referring to the function form in the literature (Etse and Willam, 1994; Grassl and Jirásek, 2006; Lu et al., 2022; Zhou et al., 2020) as follows:

$$f=\left[\left(1-H\right)\left(\frac{q}{3f_{\mathrm{c}}^{\mathrm{d}}}-\frac{p}{f_{\mathrm{c}}^{\mathrm{d}}}\right)^{2}+\frac{q}{f_{\mathrm{c}}^{\mathrm{d}}}\right]^{2}+m_{0}^{\mathrm{d}}H^{2}\left[\frac{q}{3f_{\mathrm{c}}^{\mathrm{d}}}r(\cos\theta)-\frac{p}{f_{\mathrm{c}}^{\mathrm{d}}}\right]-H^{2} \tag{11}$$

where $f_{\mathrm{c}}^{\mathrm{d}}$ and m_{0}^{d} indicate the dynamic uniaxial compressive strength and dynamic friction parameter respectively. p, q, and θ are the hydrostatic pressure, the generalized shear stress, and the stress Lode angle (Lu et al., 2022) respectively. $p=\boldsymbol{\sigma}:\boldsymbol{\delta}/3$, $q=\sqrt{3J_2}$, and $\theta=\arccos\left(3\sqrt{3}J_3/2J_2^{3/2}\right)/3$, in which J_2 and J_3 are the second and third invariants, respectively, of the deviatoric stress tensor $\mathbf{s}$. $J_2=\mathbf{s}:\mathbf{s}/2$, $J_3=\mathbf{s}^3:\boldsymbol{\delta}/3$, and $\mathbf{s}=\boldsymbol{\sigma}-p\boldsymbol{\delta}$. $\boldsymbol{\delta}$ is Kronecker delta. The function $r(\cos\theta)$ is expressed by:

$$r\left(\cos\theta\right)=\frac{4\left[1-\left(e^{\mathrm{d}}\right)^{2}\right]\cos^{2}\theta+\left[2e^{\mathrm{d}}-1\right]^{2}}{2\left[1-\left(e^{\mathrm{d}}\right)^{2}\right]\cos\theta+\left[2e^{\mathrm{d}}-1\right]\sqrt{4\left[1-\left(e^{\mathrm{d}}\right)^{2}\right]\cos^{2}\theta+5\left(e^{\mathrm{d}}\right)^{2}-4e^{\mathrm{d}}}} \tag{12}$$

where e^{d} is the dynamic eccentricity parameter. The three material parameters in the yield function, namely $f_{\mathrm{c}}^{\mathrm{d}}$, m_{0}^{d}, and e^{d}, can be obtained by the basic dynamic strength parameters, namely $f_{\mathrm{c}}^{\mathrm{d}}$, $f_{\mathrm{t}}^{\mathrm{d}}$, and $f_{\mathrm{bc}}^{\mathrm{d}}$:

$$m_{0}^{\mathrm{d}}=3\frac{\left(f_{\mathrm{c}}^{\mathrm{d}}\right)^{2}-\left(f_{\mathrm{t}}^{\mathrm{d}}\right)^{2}}{f_{\mathrm{c}}^{\mathrm{d}}f_{\mathrm{t}}^{\mathrm{d}}}\frac{e^{\mathrm{d}}}{e^{\mathrm{d}}+1} \tag{13}$$

$$e^{\mathrm{d}}=\frac{1+\acute{U}^{\mathrm{d}}}{2-\acute{U}^{\mathrm{d}}} \tag{14}$$

$$\acute{U}^{\mathrm{d}}=\frac{f_{\mathrm{t}}^{\mathrm{d}}}{f_{\mathrm{bc}}^{\mathrm{d}}}\frac{\left(f_{\mathrm{bc}}^{\mathrm{d}}\right)^{2}-\left(f_{\mathrm{c}}^{\mathrm{d}}\right)^{2}}{\left(f_{\mathrm{c}}^{\mathrm{d}}\right)^{2}-\left(f_{\mathrm{t}}^{\mathrm{d}}\right)^{2}} \tag{15}$$

where $f_{\mathrm{t}}^{\mathrm{d}}$ denotes dynamic uniaxial tensile strength and $f_{\mathrm{bc}}^{\mathrm{d}}$ indicates dynamic equibiaxial compressive strength. It is possible to write $f_{\mathrm{bc}}^{\mathrm{d}}$ as a function of $f_{\mathrm{c}}^{\mathrm{d}}$, i.e., $f_{\mathrm{bc}}^{\mathrm{d}}=h\cdot f_{\mathrm{c}}^{\mathrm{d}}$, where *h* is a constant (Wang et al., 2018). The strain rate is introduced into the yield function as a constitutive variable by strength parameters. Experimental data (Yu et al., 2013) show that at very high strain rates, the dynamic strength will inevitably approach a limit value. Therefore, the S-shaped dynamic increase factor (DIF), which can reasonably reflect the ultimate dynamic strength of concrete, is adopted to describe the proportional relationship between the static and dynamic strength parameters under uniaxial conditions (Lu et al., 2017). Appendix I presents the expression of the DIF.

The yield function is a four-dimensional (4D) hypersurface in the $(p,q,\theta,u_{\mathrm{d}})$ coordinate space. u_{d} is the logarithm of the generalized shear strain rate expressed in Eq. (25). The 4D hypersurface can be decomposed into two 3D yield surfaces in the (u_{d},p,q) and $(u_{\mathrm{d}},x_{\sigma}=q\cdot\sin\theta,y_{\sigma}=q\cdot\cos\theta)$ coordinate spaces. Fig. 3(a) presents the 3D yield surface in the (u_{d},p,q) coordinate space by setting θ equal to a constant. The yield surface's variation trend with the strain rate in the meridian plane is compatible with the evolution law of the adopted dynamic strength criterion (see Appendix I), which has an S-shaped shape and will not expand indefinitely. As illustrated in Fig. 3(b), the $(u_{\mathrm{d}},x_{\sigma},y_{\sigma})$ coordinate space can present the evolution of the yield curve with the strain rate in the deviatoric space when p is constant.

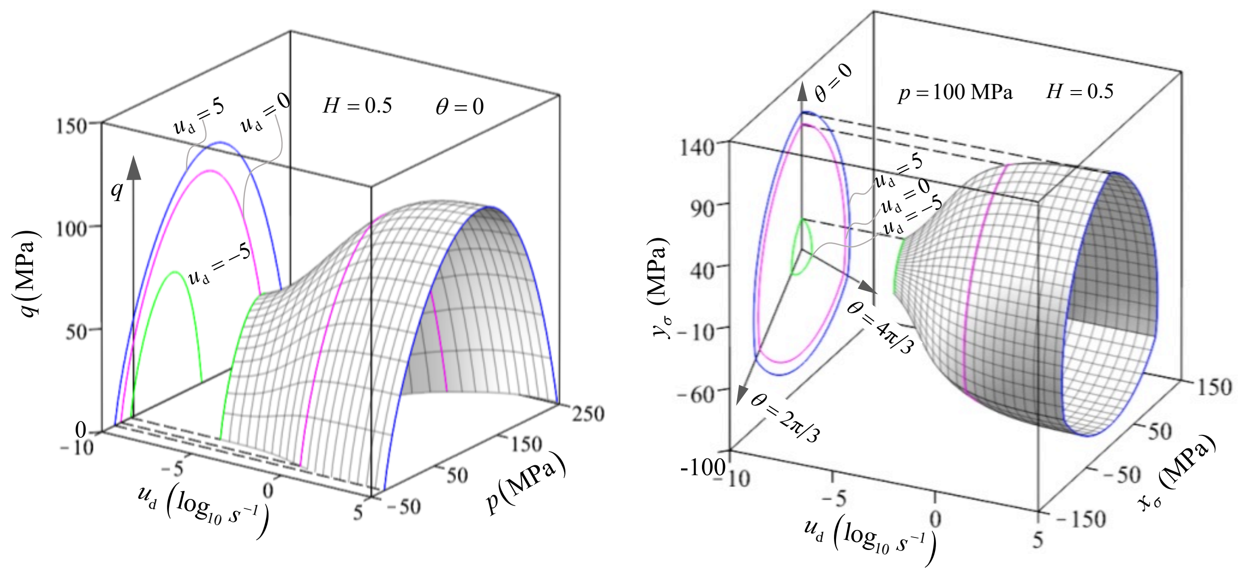

(a) yield surface in (u_{d},p,q) coordinate space (b) yield surface in $(u_{\mathrm{d}},x_{\sigma},y_{\sigma})$ coordinate space

Fig. 3. Evolution of yield surface with strain rate.

Hardening parameter

The hardening–softening parameter (H) controls the shape of the yield surface and is defined (Wang et al., 2018) as:

$$H=\frac{Ax+(D-1)x^{2}}{1+(A-2)x+Dx^{2}} \tag{16}$$

where H simultaneously describes the deformation behavior of concrete in the hardening and softening stages. When $H = 1$, the yield surface in Eq. (11) is degenerated into an open strength surface, as shown in Fig. 4. A and D are the model parameters. x is a plastic internal variable, and $x = \varepsilon_{\mathrm{d}}^{\mathrm{p}} / \varepsilon_{\mathrm{ds}}^{\mathrm{p}}$. $\varepsilon_{\mathrm{d}}^{\mathrm{p}}$ indicates the equivalent plastic shear strain. $\varepsilon_{\mathrm{ds}}^{\mathrm{p}}$ is the value of $\varepsilon_{\mathrm{d}}^{\mathrm{p}}$ at peak stress. The test data (Candappa et al., 2001; Imran and Pantazopoulou, 1996; Kupfer et al., 1969; Lu and Hsu, 2007) reveal that parameters $\varepsilon_{\mathrm{ds}}^{\mathrm{p}}$ and A (cf. Fig. 5) correlate with the stress state as follows:

$$\frac{\varepsilon_{\mathrm{ds}}^{\mathrm{p}}}{\varepsilon_{1,\mathrm{ds}}^{\mathrm{p}}} = \frac{14.70}{1 + e^{\ln(13.70) + 2.30 - 2.30 \cdot \left(\frac{q_{\max}}{f_{\mathrm{c}}}\right)}} \tag{17}$$

$$\frac{A}{A_1} = \frac{3.88}{1 + e^{\ln(2.88) + 2.22 - 2.22 \cdot \left(\frac{q_{\max}}{f_{\mathrm{c}}}\right)}} \tag{18}$$

where $\varepsilon_{1,\mathrm{ds}}^{\mathrm{p}}$ and A_1 are the value of $\varepsilon_{\mathrm{ds}}^{\mathrm{p}}$ and A under uniaxial compressive conditions respectively. The physical meaning of A can be found in ref (Wang et al., 2018). $q_{\max}$ is the largest q in loading history.

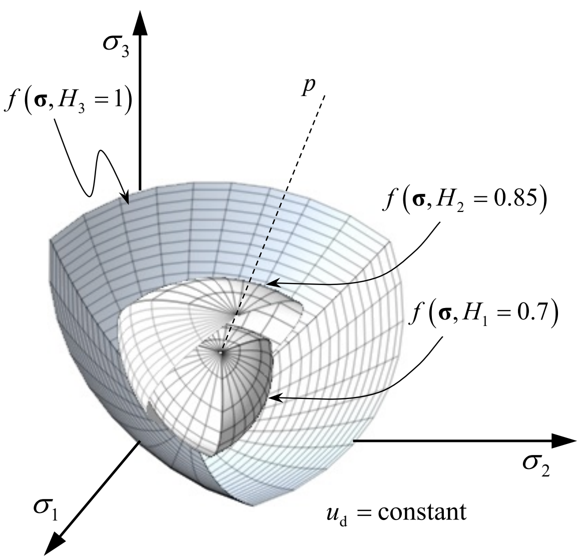

Fig. 4. Evolution of yield surface with H when u_{d} is constant.

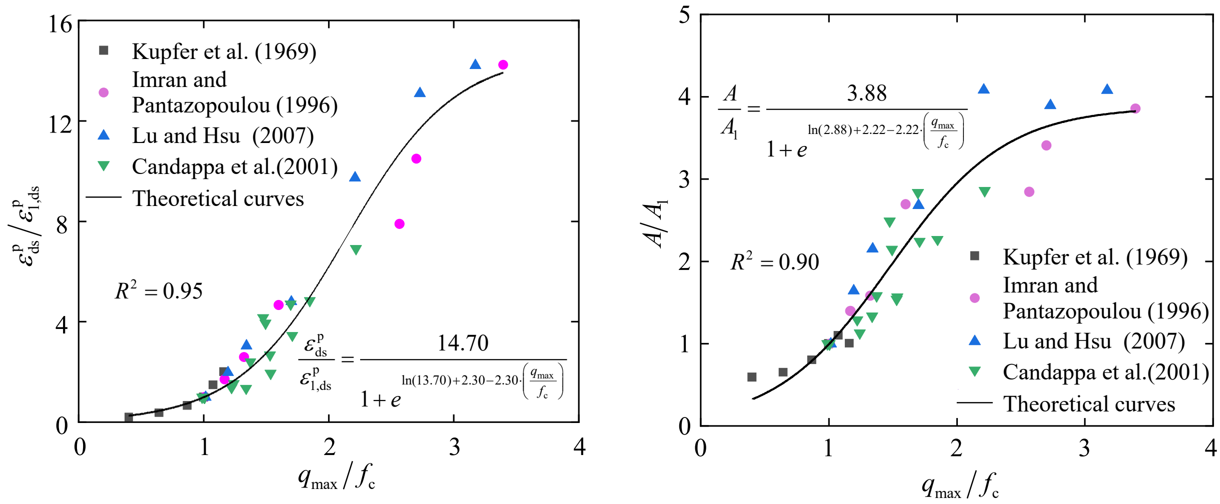

(a) ε_{ds}^{p} with the stress state (b) A with the stress state

Fig. 5. Relationship of material parameters with the stress state.

Flow rule

A non-orthogonal flow rule (Lu et al., 2019; Lu et al., 2022) is employed, which directly determines $\mathbf{r}$ in Eq. (7) via the developed dynamic yield function:

$$\mathbf{r} = \frac{\partial^{\mu} f}{\partial p^{\mu}}\frac{\partial p}{\partial \boldsymbol{\sigma}} + \frac{\partial^{\mu} f}{\partial q^{\mu}}\frac{\partial q}{\partial \boldsymbol{\sigma}} \tag{19}$$

where μ indicates the fractional order and $\partial^{\mu} f/\partial(\cdot)^{\mu}$ is the Riemann–Liouville fractional derivative operator, the details of which can be found in ref (Lu et al., 2022). $\partial p/\partial\boldsymbol{\sigma} = \boldsymbol{\delta}/3$ and $\partial q/\partial\boldsymbol{\sigma} = 1.5\mathbf{s}/q$ are used to achieve the conversion of coordinates from principal stress to general stress, the expressions of which can be found in Eqs. (36) and (39). Combining with Eq. (11), $\partial^{\mu} f/\partial p^{\mu}$ and $\partial^{\mu} f/\partial q^{\mu}$ can be obtained:

$$\begin{cases} \dfrac{\partial^{\mu} f}{\partial p^{\mu}} = \dfrac{a_0 p^{-\mu}}{\Gamma(1-\mu)} + \dfrac{a_1\Gamma(2)p^{1-\mu}}{\Gamma(2-\mu)} + \dfrac{a_2\Gamma(3)p^{2-\mu}}{\Gamma(3-\mu)} + \dfrac{a_3\Gamma(4)p^{3-\mu}}{\Gamma(4-\mu)} + \dfrac{a_4\Gamma(5)p^{4-\mu}}{\Gamma(5-\mu)} \\ \dfrac{\partial^{\mu} f}{\partial q^{\mu}} = \dfrac{b_0 q^{-\mu}}{\Gamma(1-\mu)} + \dfrac{b_1\Gamma(2)q^{1-\mu}}{\Gamma(2-\mu)} + \dfrac{b_2\Gamma(3)q^{2-\mu}}{\Gamma(3-\mu)} + \dfrac{b_3\Gamma(4)q^{3-\mu}}{\Gamma(4-\mu)} + \dfrac{b_4\Gamma(5)q^{4-\mu}}{\Gamma(5-\mu)} \end{cases} \tag{20}$$

where $\Gamma(\cdot)$ is the gamma function. Coefficients a_i and b_i $(i = 0, 1, 2, 3, 4)$ are given as follows respectively.

$$
\begin{cases}
a_0 = \dfrac{(1-H)^2 q^4}{81\left(f_c^d\right)^4} + \dfrac{2(1-H)q^3}{9\left(f_c^d\right)^3} + \dfrac{q^2}{\left(f_c^d\right)^2} + \dfrac{m_0^d H^2 r(\cos\theta) q}{3 f_c^d} - H^2 \\
a_1 = -\dfrac{4(1-H)^2 q^3}{27\left(f_c^d\right)^4} - \dfrac{4(1-H)q^2}{3\left(f_c^d\right)^3} - \dfrac{m_0^d H^2}{f_c^d} \\
a_2 = \dfrac{2(1-H)^2 q^2}{3\left(f_c^d\right)^4} + \dfrac{2(1-H)q}{\left(f_c^d\right)^3} \\
a_3 = -\dfrac{4(1-H)^2 q}{3\left(f_c^d\right)^4} \\
a_4 = \dfrac{(1-H)^2}{\left(f_c^d\right)^4}
\end{cases}
\tag{21}
$$

$$
\begin{cases}
b_0 = \dfrac{(1-H)^2 p^4}{\left(f_c^d\right)^4} - \dfrac{m_0^d H^2 p}{f_c^d} - H^2 \\
b_1 = -\dfrac{4(1-H)^2 p^3}{3\left(f_c^d\right)^4} + \dfrac{2(1-H)p^2}{\left(f_c^d\right)^3} + \dfrac{m_0^d H^2 r(\cos\theta)}{3 f_c^d} \\
b_2 = \dfrac{2(1-H)^2 p^2}{3\left(f_c^d\right)^4} - \dfrac{4(1-H)p}{3\left(f_c^d\right)^3} + \dfrac{1}{\left(f_c^d\right)^2} \\
b_3 = -\dfrac{4(1-H)^2 p}{27\left(f_c^d\right)^4} + \dfrac{2(1-H)}{9\left(f_c^d\right)^3} \\
b_4 = \dfrac{(1-H)^2}{81\left(f_c^d\right)^4}
\end{cases}
\tag{22}
$$

The constitutive equation of the established model can be obtained by substituting Eqs. (11), (16) and (19) into the incremental stress–strain–environment relation in Eq. (7). Appendix II presents the details of the derivation process.

Loading–unloading criterion

This section introduces the environmental variable u_d into the yield function as a constitutive variable. The loading–unloading criterion under the combined action of $\boldsymbol{\varepsilon}$ and u_d can be presented based on Eq. (9) in the $\left(\boldsymbol{\varepsilon}, u_d\right)$ coordinate space as follows:

$$\frac{\partial F}{\partial \boldsymbol{\varepsilon}} : \mathrm{d}\boldsymbol{\varepsilon} + \frac{\partial F}{\partial u_{\mathrm{d}}} \mathrm{d}u_{\mathrm{d}} = \begin{cases} \dfrac{\partial f}{\partial \boldsymbol{\sigma}} : \mathbf{D}^{\mathrm{e}} : \mathrm{d}\boldsymbol{\varepsilon} + \dfrac{\partial f}{\partial u_{\mathrm{d}}} \mathrm{d}u_{\mathrm{d}} > 0 & \text{Loading} \\ \dfrac{\partial f}{\partial \boldsymbol{\sigma}} : \mathbf{D}^{\mathrm{e}} : \mathrm{d}\boldsymbol{\varepsilon} + \dfrac{\partial f}{\partial u_{\mathrm{d}}} \mathrm{d}u_{\mathrm{d}} = 0 & \text{Neutral loading} \\ \dfrac{\partial f}{\partial \boldsymbol{\sigma}} : \mathbf{D}^{\mathrm{e}} : \mathrm{d}\boldsymbol{\varepsilon} + \dfrac{\partial f}{\partial u_{\mathrm{d}}} \mathrm{d}u_{\mathrm{d}} < 0 & \text{Unloading} \end{cases} \tag{23}$$

where $\left(\partial F/\partial \boldsymbol{\varepsilon}, \partial F/\partial u_{\mathrm{d}}\right)$ represents the dynamic closed yield surface's normal direction.

Model analysis

To analyze the effect of strain rate as a constitutive variable, a loading path with reduced strain rate and constant stress similar to the creep process is discussed as an example for model analysis. Table 1 shows the model parameters used in the model analysis, where the dynamic strength parameters' statistical values and other parameters are obtained by referring to the concrete test (Kupfer et al., 1969; Lu et al., 2017). During the creep evolution, the stress remains constant and the total strain increases gradually. Constant stress makes the elastic strain increment zero, so the increase in total strain is due to an increase in plastic strain. This phenomenon is consistent with that described by Eq. (6), that is, the plastic strain caused by environmental changes will occur even under constant stress conditions. The plastic strain drives the evolution of H as an internal variable. The relationship between the H and the u_{d} and axial stress σ_1 under the uniaxial compression condition is depicted in Fig. 6. The initial point N_1 is loaded to $H = 0.3$ under the condition of $u_{\mathrm{d}} = 4$. Similar test conditions for the discussed loading path N_1N_2 have been studied for high-density polyethylene (Reis et al., 2014). According to Eq. (6), the material will produce plastic deformation as a result of the change in strain rate. The accumulation of plastic deformation causes the hardening parameter to increase from 0.3 to 0.84. At this time, the yield surface will expand outward correspondingly with the increase of H. Fig. 7 shows the yield surfaces at the two state points N_1 and N_2, and the four-dimensional hypersurface is still displayed by two three-dimensional surfaces. As seen in Fig. 7, the yield surface's expansion makes the new state point N_2 still on the subsequent yield surface, which means that the consistency condition is strictly satisfied. By taking into consideration the strain rate dimension, the yield surface expansion caused by a change in strain rate can be captured.

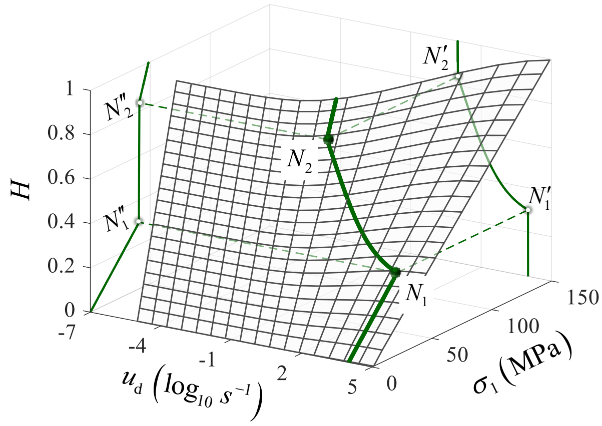

Fig. 6. The influence of strain rate and stress on the evolution of hardening parameter.

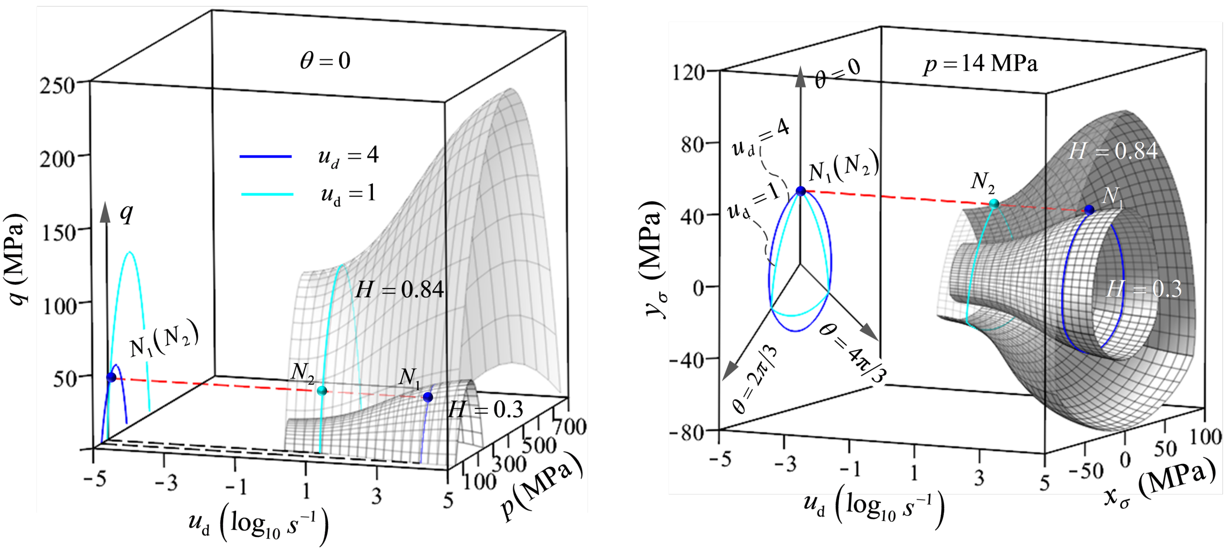

(a) yield surface in (u_d, p, q) coordinate space (b) yield surface in $(u_d, x_\sigma, y_\sigma)$ coordinate space

Fig. 7. Influence of strain rate change on yield surface evolution.

Table 1

The model parameters for analysis.

E (MPa)	ν	f_c (MPa)	$\mathrm{DIF}_{c,max}$	ξ_c	$\mathrm{DIF}_{t,max}$	ξ_t	$\varepsilon^{p}_{1,ds}$	A_1	D	μ
30000	0.2	32.8	4.72	1.2	16	1.4	0.003	10	0.8	1.90

Test of loading under constant- and variable-strain rate

Two types of constant- and variable-strain rate loading experiments are conducted in the Rapid Triaxial Testing Systems of Beijing University of Technology. The variable strain rate loading tests are conducted under uniaxial compressive conditions. The constant-strain rate tests are performed under conventional triaxial compressive conditions.

Testing procedures and apparatus

The loading process at a constant-strain rate is realized by setting the linear relationship of axis strain to time, including four strain rates, i.e., $\dot{\varepsilon}_1$ of 10^{-5} s^{-1}, 10^{-4} s^{-1}, 10^{-3} s^{-1}, and 10^{-2} s^{-1}, and three confining pressures, i.e., σ_3 of 0 MPa, 10 MPa, and 20 MPa. The concrete specimen is first subjected to the confining pressure at a rate of 5 MPa/min, during which the synchronous increase of axial stress makes the specimen in the isotropic stress state. The confining pressure remains constant after target value is achieved. Then, utilizing displacement control, the axial loading is applied until the test is finished. For another set of dynamic tests with variable strain rate loading, the axial strain changes with time as a quadratic function, that is, the axial strain rate increases linearly with time. In the three sets of variable-strain rate tests, the strain rate increment is 10^{-7} s^{-2}, 10^{-5} s^{-2}, and 10^{-3} s^{-2}, respectively.

All dynamic loading tests were performed on the Rapid Triaxial Testing Systems (RTR-1500) shown in Fig. 8(a). It primarily comprises a fast pulse decay permeability apparatus, a confining pressure intensifier apparatus, a pore pressure intensifier apparatus, a digital-signal conditioning control unit, and high-pressure triaxial cells. Its compressive loading capacity is up to 1500 kN, and the confining pressure and pore pressure can be increased to 140 MPa. Fig. 8(b) shows the measuring device of axial strain and lateral strain respectively. The axial strain is calculated by the gauge axial deformation and the axial gauge length of the specimen. The strain hinge measures the lateral strain. The length of the strain hinge can be adjusted according to the specimen, and the testing system automatically converts the lateral strain according to the change in the hinge circumference.

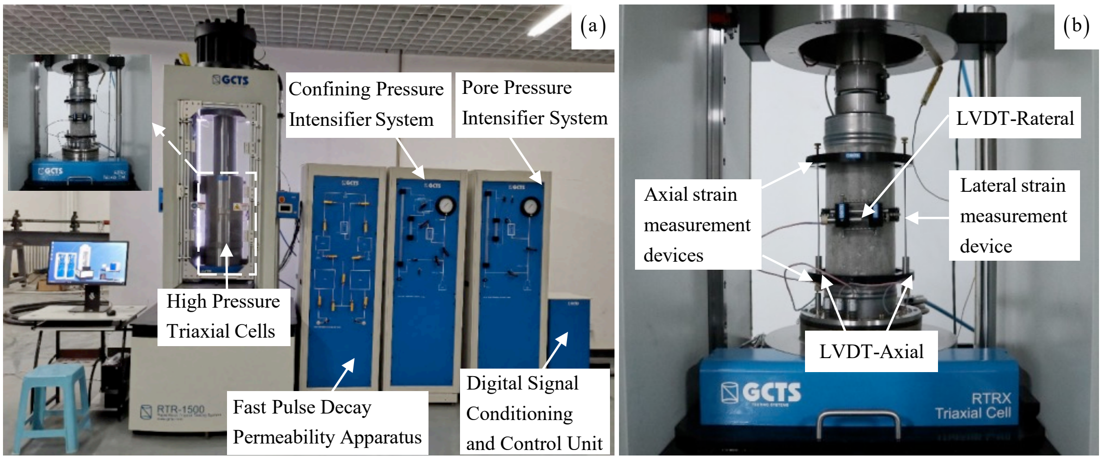

Fig. 8. A schematic of the testing system: (a) Rapid Triaxial Rock Testing Systems; (b) devices for measuring the axial and lateral strains.

Preparation of materials and specimens

Table 2 lists the mixed proportion of the concrete, and the cementitious materials are 42.5 ordinary Portland cement. Crushed stone with a diameter of 5 to 20 mm makes up the coarse aggregate, while medium sand with a fineness modulus of 2.42 makes up the fine aggregate. First, materials for preparing mortar mixture are prepared according to the mix proportion. Then, the coarse and fine aggregates are mixed with the cement evenly. The tap water is gradually added to the mixture during the stirring. The well-mixed concrete is cast into a mold coated with a release agent and vibrated to a compact state on a vibrating table. All the specimens are demolded after curing for 24 h at room temperature. After demolding, the specimens are further cured for 28 days in a standard curing room.

Table 2

The mixture proportion of the concrete.

Cement (kg/m³)	Fine aggregate (kg/m³)	Coarse aggregate (kg/m³)	Water (kg/m³)	Water-to-cement ratio
389	554	1196	190	0.49

Experimental results

The experimental results of constant-strain rate and variable-strain rate are given respectively.

Constant-strain rate

Table III.1 in Appendix III summarizes the test results for all specimens. Fig. 9 displays the stress-strain curves for each specimen at varied confining pressures and strain rates. The peak deviatoric stress $(\sigma_1 - \sigma_3)^{\mathrm{p}}$ can be used to characterize the shear strength of concrete under conventional triaxial compression conditions. It can be found that the $(\sigma_1 - \sigma_3)^{\mathrm{p}}$ rises as confining pressure and strain rate increase due to restraint strengthening effect and strain rate effect of concrete. Numerous studies have delved into exploring the mechanism behind the increase in strength of concrete materials resulting from strain rate effects. According to consensus, the thermal activation mechanism, the Stefan effect, and inertial mechanisms are responsible for enhancing the overall load-bearing capacity of concrete at a macroscopic level (Lu et al., 2017; Qi et al., 2009; Zhang and Zhao, 2014). The thermal activation mechanism is caused by the thermal motion of atoms, which plays a role in the whole strain rate range. The latter two mechanisms only play within the range of medium to high strain rates. For the strain rates range tested, the strength of concrete increased due to the combined effects of thermal activation and the Stefan effect, with the former playing a more prominent role. The strain at the peak stress under conventional triaxial conditions significantly increase compared to the uniaxial condition at the same loading rate. The results show that the confining pressure improves the ductility and resistance of concrete to deformation.

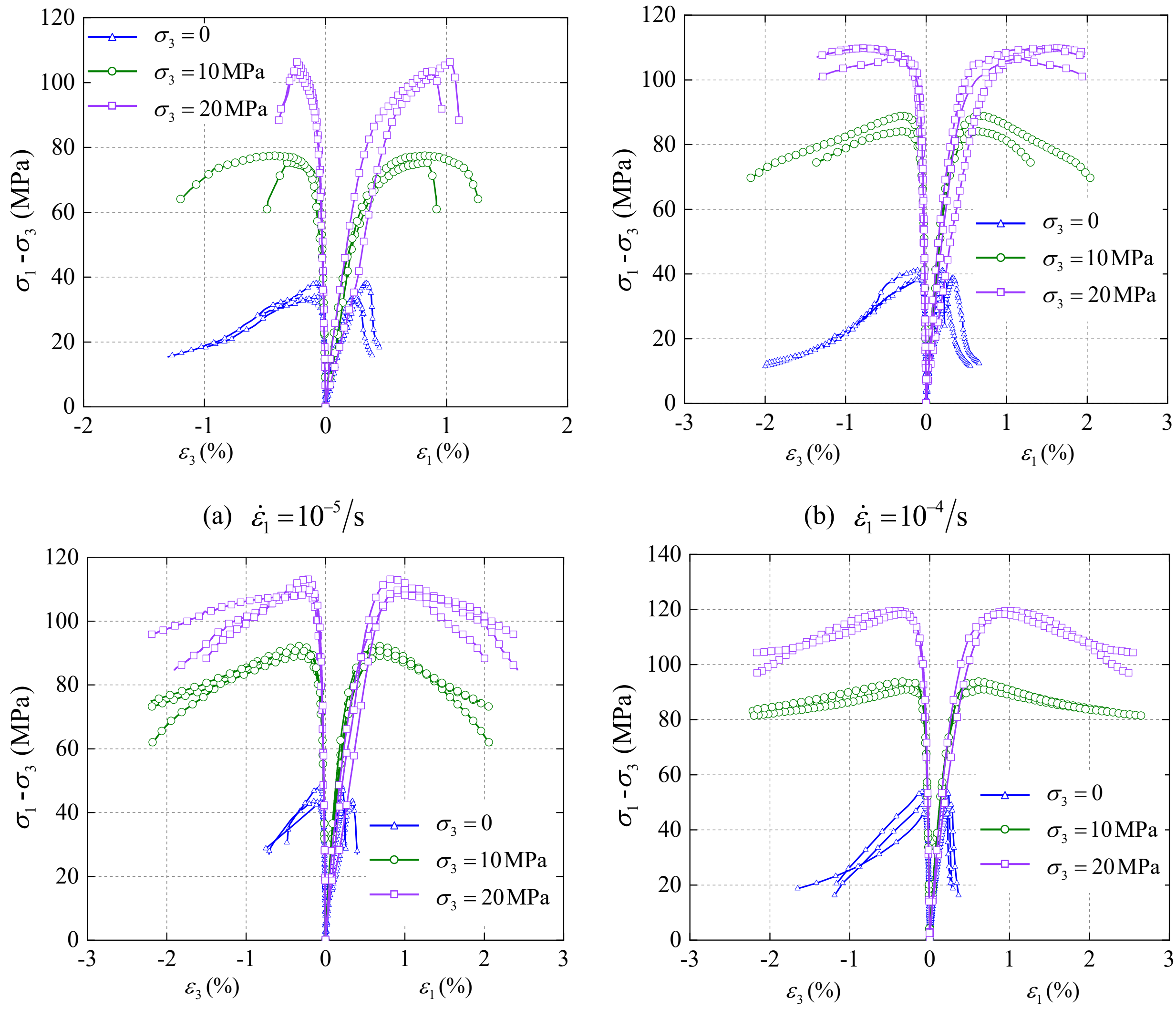

(a) $\dot{\varepsilon}_1 = 10^{-5}/\mathrm{s}$ (b) $\dot{\varepsilon}_1 = 10^{-4}/\mathrm{s}$

(c) $\dot{\varepsilon}_1 = 10^{-3}/\mathrm{s}$ (d) $\dot{\varepsilon}_1 = 10^{-2}/\mathrm{s}$

Fig. 9. Curves of stress–strain at different constant strain rates.

Variable-strain rate

The actual loading process is obtained through the strain–time data points automatically collected by the testing instrument during the loading process (see Fig. 10(b), (d), and (f)). The strain rate increments of three groups of variable-strain rate tests are 1.26×10^{-7} s^{-2}, 1.26×10^{-5} s^{-2}, and 8.8×10^{-4} s^{-2} respectively. The $\sigma_1-\varepsilon_1-\dot{\varepsilon}_1$ and $\sigma_1-\varepsilon_3-\dot{\varepsilon}_1$ behavior is depicted in Fig. 10(a), (c), and (e), where each working condition is repeated three times. The $\dot{\varepsilon}_1$, σ_1, ε_1, and ε_3 at the peak stress are all listed in Table 3's summary of the test findings for all of the variable-strain rate experiments. As shown in Fig. 11, the strength of concrete increases with an increase in the strain rate increment. A larger strain rate increment means a faster increase in the strain rate.

When the strain rate changes more rapidly before reaching its peak strength, the performance of the specimen resistant to external loads will be exerted more fully.

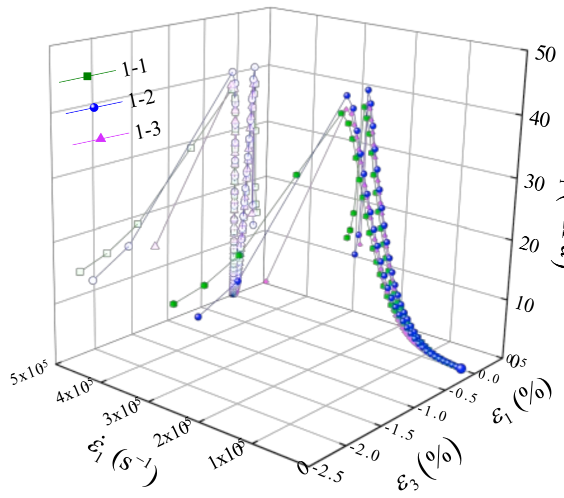

(a) $\sigma_1-\varepsilon_1-\dot{\varepsilon}_1$ and $\sigma_1-\varepsilon_3-\dot{\varepsilon}_1$ curves of group one

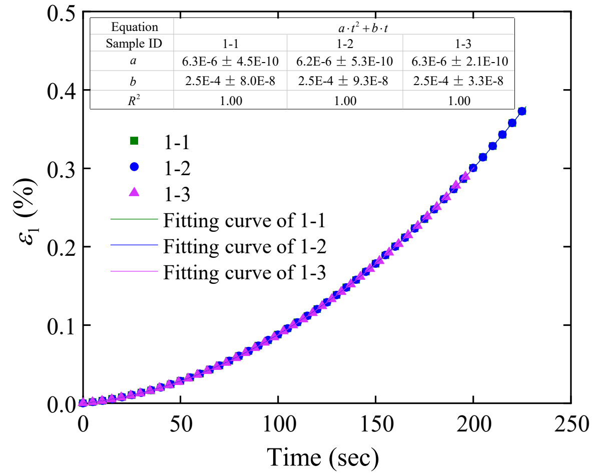

(b) strain–time curves of group one

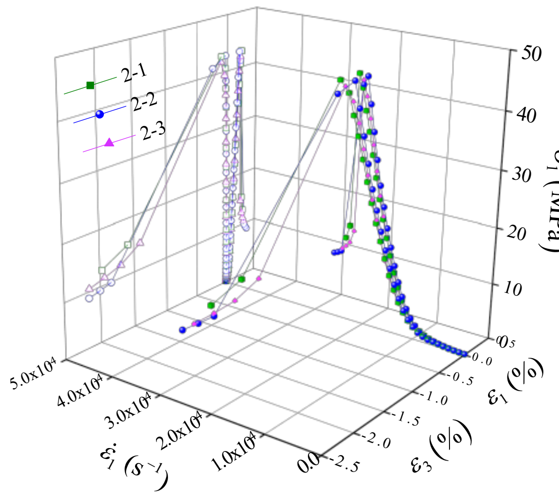

(c) $\sigma_1-\varepsilon_1-\dot{\varepsilon}_1$ and $\sigma_1-\varepsilon_3-\dot{\varepsilon}_1$ curves of group two

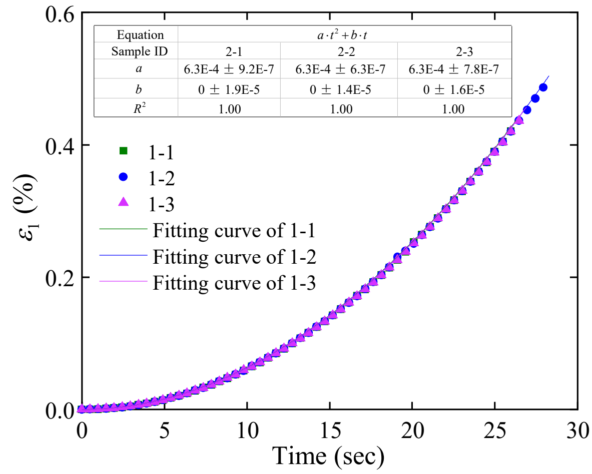

(d) strain–time curves of group two

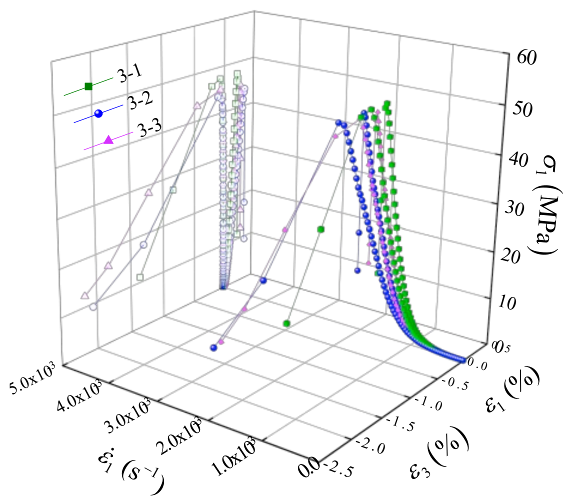

(e) $\sigma_1-\varepsilon_1-\dot{\varepsilon}_1$ and $\sigma_1-\varepsilon_3-\dot{\varepsilon}_1$ curves of group three

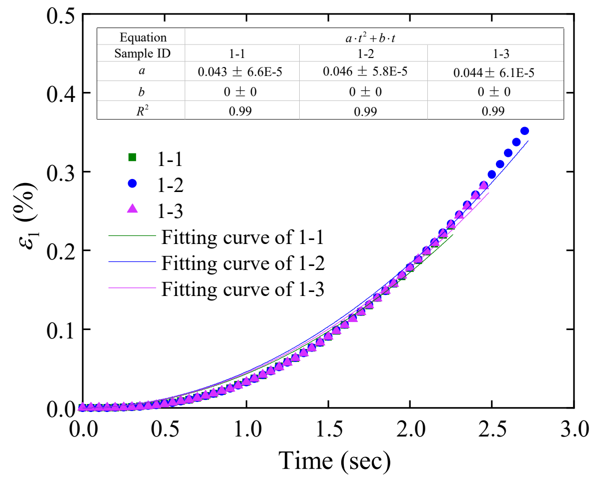

(f) strain–time curves of group three

Fig. 10. Stress–strain–strain rate curves and strain–time curves during loading.

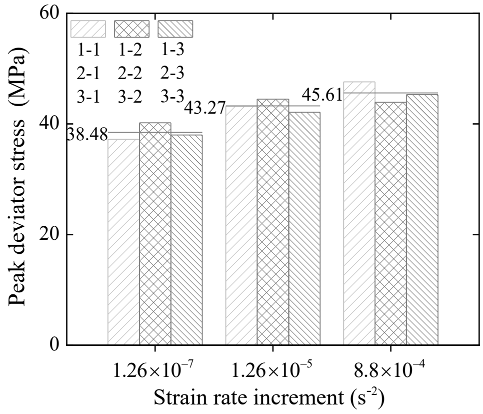

Fig. 11 Strength value in different strain rate increment.

Table 3

The test results at different variable-strain rates.

Sample Group	Sample ID	H × D (mm × mm)	$\dot{\varepsilon}_1$ at peak stress (s^{-1})	σ_1 (MPa)	ε_1 at peak stress (%)	ε_3 at peak stress (%)	Average Stress (MPa)
	1-1	199.79 × 99.10	2.7×10^{-5}	37.22	0.2869	−0.0899	
1	1-2	199.30 × 99.09	2.6×10^{-5}	40.22	0.2702	−0.0848	38.48
	1-3	199.32 × 99.07	2.6×10^{-5}	38.01	0.2649	−0.0823	
	2-1	199.35 × 99.10	2.5×10^{-4}	43.21	0.2420	−0.0773	
2	2-2	201.14 × 99.13	2.4×10^{-4}	44.49	0.2178	−0.0579	43.27
	2-3	199.74 × 99.04	2.4×10^{-4}	42.12	0.2312	−0.1668	
	3-1	201.30 × 99.08	1.9×10^{-3}	47.60	0.2224	−0.0808	
3	3-2	199.22 × 99.10	2.5×10^{-3}	43.92	0.3489	−0.0813	45.61
	3-3	199.53 × 98.72	2.5×10^{-3}	45.31	0.2689	−0.0993	

Evaluation of the constitutive model

The model's performance is evaluated using experimental data collected under both constant- and variable-strain rate conditions. The constant-strain rate tests include the conventional triaxial compression tests conducted by the authors and the uniaxial and biaxial compression tests obtained from published papers. The variable-strain rate conditions tests are performed by authors. In particular, a designed experiment with a sudden increase and decrease in strain rate is designed to supplement the analysis of variable-strain rate cases.

The established model has eleven parameters, including two elastic parameters (E , ν), five strength parameters (f_{c} , $\mathrm{DIF}_{\mathrm{c,max}}$, ξ_{c} , $\mathrm{DIF}_{\mathrm{t,max}}$, ξ_{t}), three parameters controlling deformation ($\varepsilon_{1,\mathrm{ds}}^{\mathrm{p}}$, A_1 , D) in the hardening-softening function, and a fractional order (μ) that captures the direction of plastic flow. E , ν and f_{c} can be obtained by uniaxial compression tests, and $f_{\mathrm{t}} = 0.1 f_{\mathrm{c}}$ (Gebbeken and Krauthammer, 2013). $\varepsilon_{1,\mathrm{ds}}^{\mathrm{p}}$ is the value of $\varepsilon_{\mathrm{ds}}^{\mathrm{p}}$ at f_{c}. Reference (Wang et al., 2018) gives expressions for determining A_1 and D. μ can be calibrated by the stress and strain at the phase transition point (Zhou et al., 2020). Reference (Lu et al., 2017) gives the determination method of the dynamic strength parameters ($\mathrm{DIF}_{\mathrm{c,max}}$, ξ_{c} , $\mathrm{DIF}_{\mathrm{t,max}}$, ξ_{t}) and also provides the statistical values of these four parameters based on the analysis of numerous compression and tension tests. Table 4 presents the model parameters adopted by the tests.

Constant-strain rate

First, the comparison results between the model and test under conventional triaxial compression conditions with σ_3 of 0 MPa, 10 MPa, and 20 MPa are evaluated. The model parameters are calibrated using test data at $\sigma_3 = 0$ MPa. These calibrated values are then used to predict test results at σ_3 of 10 MPa and 20 MPa. Fig. 12 shows the model's prediction curve and test results. According to test results, as confining pressure increases, concrete's ability to resist plastic deformation enhances, and the phenomena of softening weaken. The proposed model can well capture these experimental laws because it establishes two semi-empirical formulas for the increase of $\varepsilon_{\mathrm{ds}}^{\mathrm{p}}$ and A with increasing stress (Eqs. (17) and (18)) to characterize the impact of confining pressure on the deformation properties. In addition, as shown in Fig. 13, the test results under different confining pressures also show that the strength of concrete rises as the strain rate does. The developed dynamic strength criterion in Eq. (11) is proven to be rational by comparing the model's strength curve with the test results.

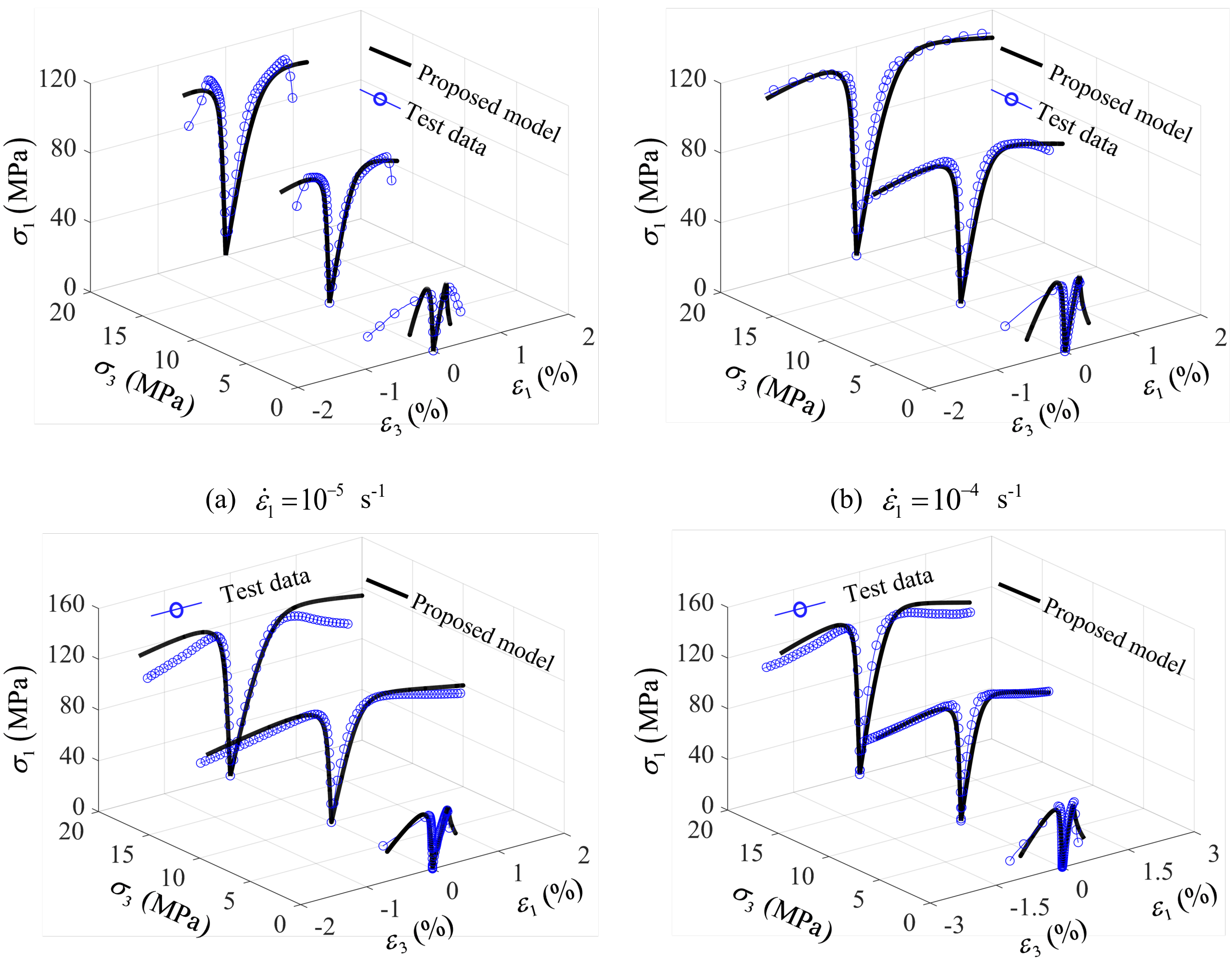

(a) $\dot{\varepsilon}_1 = 10^{-5}$ s^{-1} (b) $\dot{\varepsilon}_1 = 10^{-4}$ s^{-1}

(c) $\dot{\varepsilon}_1 = 10^{-3}$ s^{-1} (d) $\dot{\varepsilon}_1 = 10^{-2}$ s^{-1}

Fig. 12. Comparison results between the model and test under conventional triaxial compression conditions.

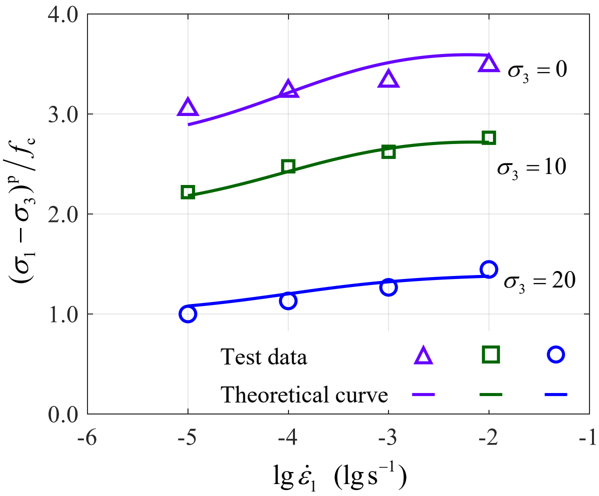

Fig. 13. Comparison of strength results between model prediction and test data.

The following evaluates the ability of the model using biaxial compressive–compressive loading tests with σ_3 of zero reported by Yin and Li (2007). The ratio of σ_2 to σ_1 is set at 0:1.0, 0.25:1.0, 0.50:1.0, 0.75:1.0, and 1.0:1.0, and the values of $\log_{10}\dot{\varepsilon}_1$ equal −5, −4, and −3. Fig. 14(a–e) illustrates the prediction results of stress versus strain at different strain rates and various stress ratios. It can be seen that the proposed model is capable of portraying the stress-strain performance of concrete when subjected to varying loading conditions. Based on the comparison of strength values between the model and experimental results in Fig. 14(f), it can be concluded that the developed yield function can accurately characterize the multiaxial dynamic strength of concrete.

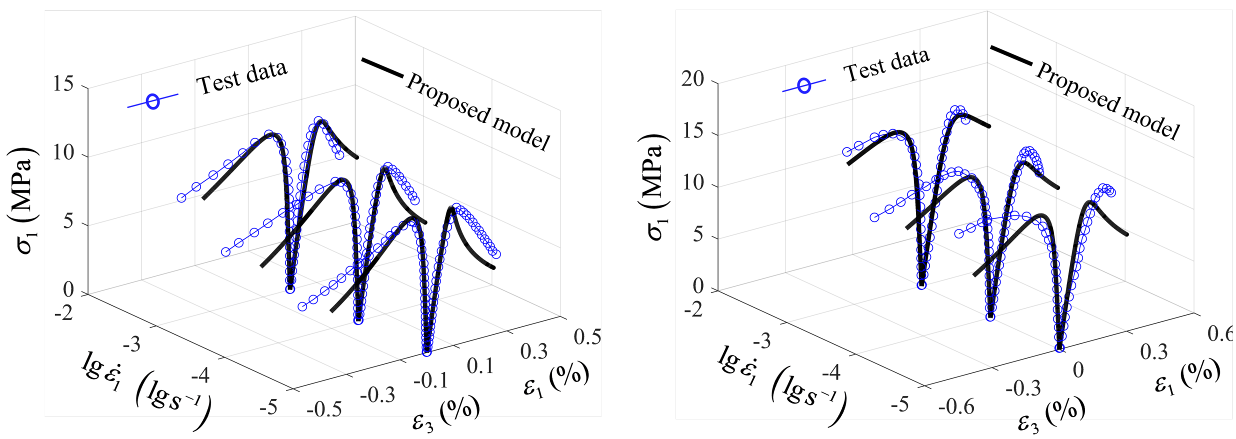

(a) $\sigma_2:\sigma_1=0.0:1.0$ (b) $\sigma_2:\sigma_1=0.25:1.0$

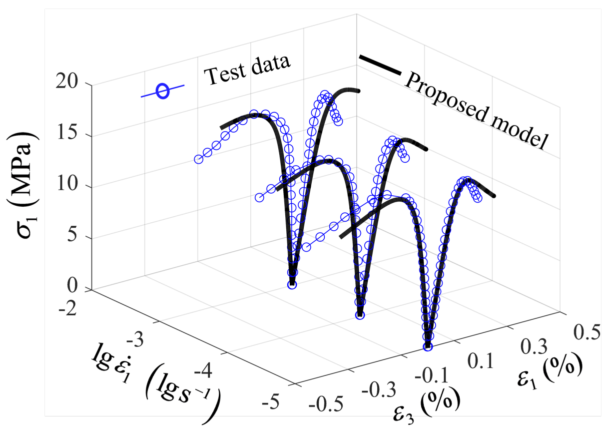

(c) $\sigma_2:\sigma_1 = 0.5:1.0$

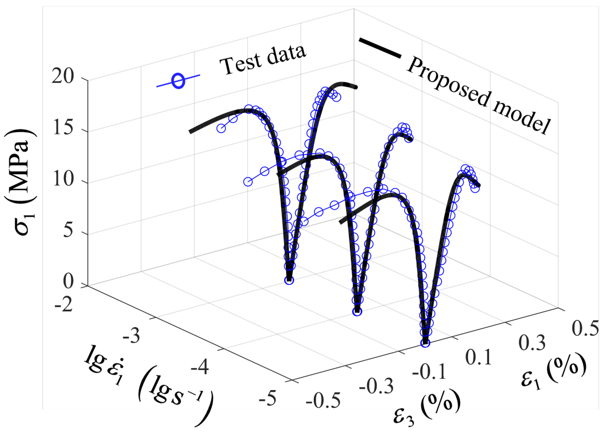

(d) $\sigma_2:\sigma_1 = 0.75:1.0$

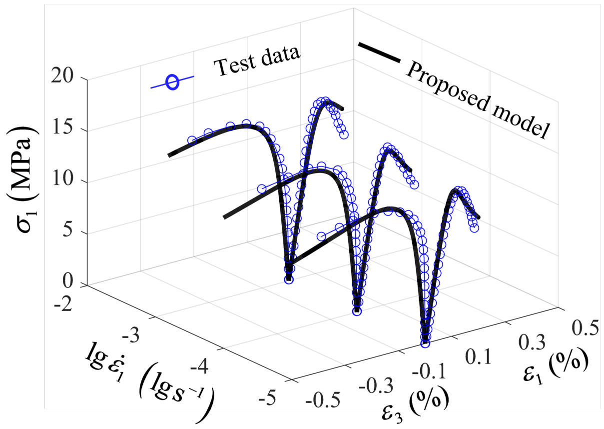

(e) $\sigma_2:\sigma_1 = 1.0:1.0$

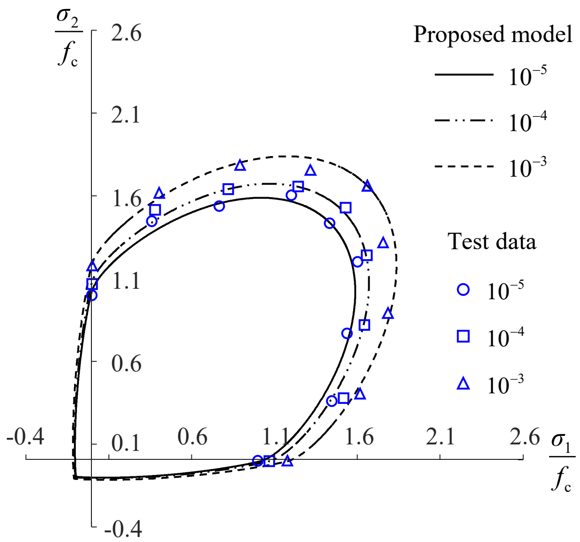

(f) value of the dynamic multiaxial strength

Fig. 14. Model predictions versus the test data for biaxial compression conducted by Yin and Li (2007).

To confirm the model's ability at high strain rates, four split Hopkinson pressure bar tests performed by Grote et al. (2001) are adopted, where $\dot{\varepsilon}_1$ equals 290 s^{-1}, 620 s^{-1},1050 s^{-1},1500 s^{-1}. When $\dot{\varepsilon}_1 = 1500\,\text{s}^{-1}$, dynamic strength f_c^d, nearly 3.5 times the static strength f_c, is 160MPa. This indicates that there is a significant increase in compressive strength with an increase in $\dot{\varepsilon}_1$. A comparison is shown in Fig. 15 between the $\sigma_1 - \varepsilon_1$ curve of the predicted and tested results. The prediction results show that the proposed model can describe concrete behavior at high strain rates.

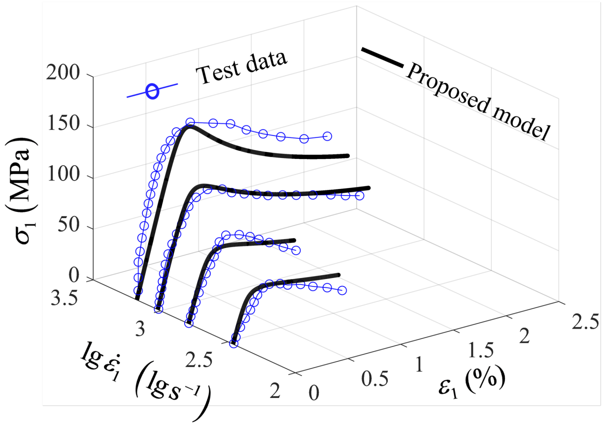

Fig. 15. Comparing the model predictions with the test results at high strain rates.

Variable-strain rate

To further evaluate the capabilities of the developed model, the test data under variable-strain rate loading conditions are adopted to compare with the model simulation results. Fig. 16 illustrates the comparison results between model predictions and test data in the stress–strain–strain rate coordinate space. The changes in strain rate during loading are evident from the curve depicted on the strain and strain rate plane in Fig. 16, which is different from a constant strain rate. At this time, the specimen is subject to the combined action of strain and strain rate. The comparison results demonstrate that the model can predict the stress–strain–strain rate relationship of concrete under different strain rate increments conditions.

The variable strain rate test is conducted only with a slowly increasing strain rate due to limitations in test conditions. To highlight the performance of the proposed model, a designed dynamic loading test is analyzed, in which the strain rate sharply decreases from 1000 s^{-1} to 1 s^{-1} during the A_1A_2 loading path (see Fig. 17). The variable strain rate test results of composite materials have shown that a reduction in strain rate will result in a corresponding reduction in stress during the loading process (Khan and Liu, 2012; Reis et al., 2014). A dynamic stress–strain model ignoring strain rate increments is also employed as a comparison in which strain rate is only the influencing factor of material parameters rather than a constitutive variable. *f*, *H*, and flow rule of the dynamic stress–strain model are the same as those used in the proposed models.

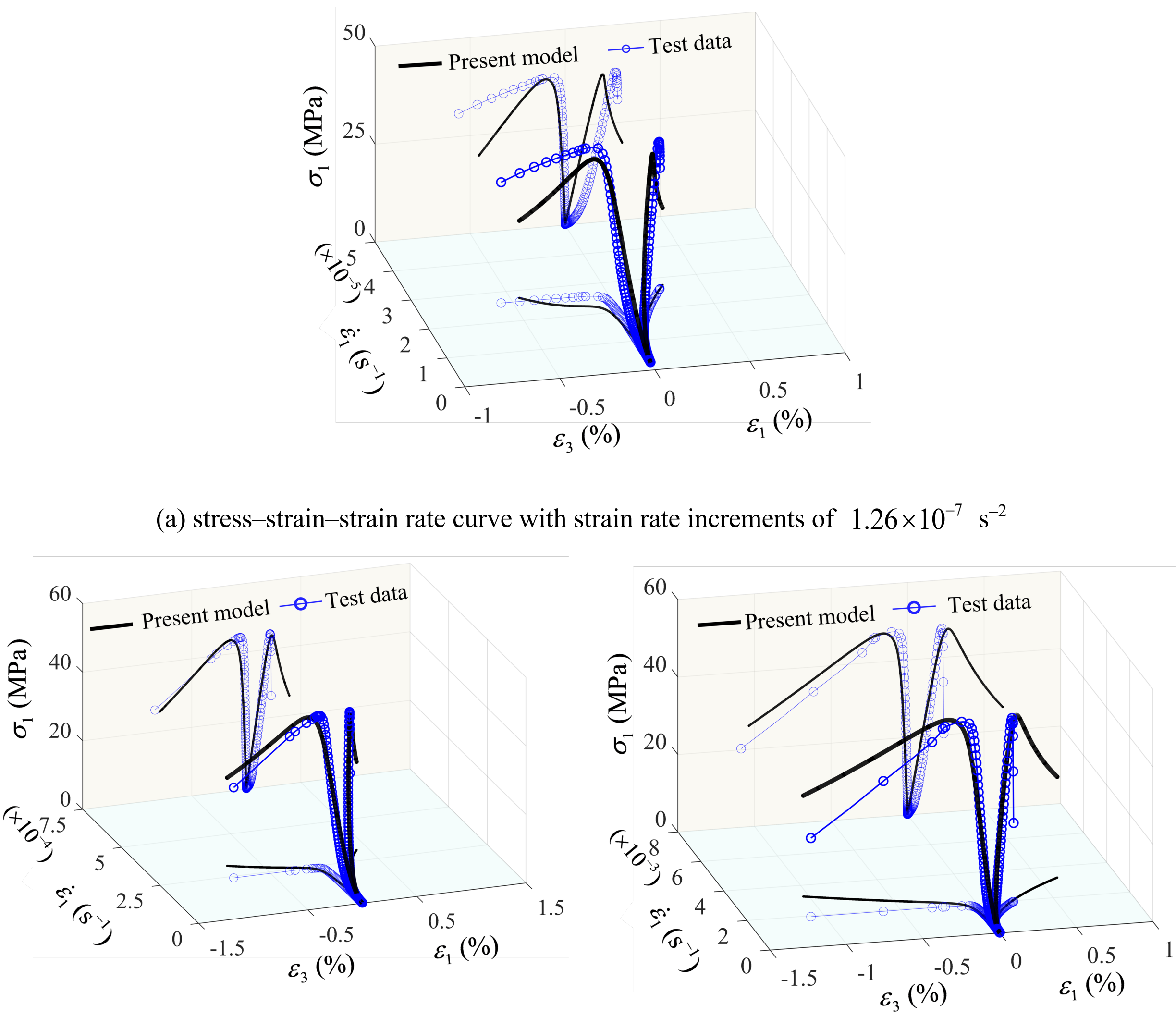

(a) stress–strain–strain rate curve with strain rate increments of 1.26×10^{-7} s^{-2}

(b) stress–strain–strain rate curve with strain rate increments of 1.26×10^{-5} s^{-2}

(c) stress–strain–strain rate curve with strain rate increments of 8.8×10^{-4} s^{-2}

Fig. 16. Comparing the model predictions with the test results under different strain rate increments conditions.

Fig. 17 shows the stress–plastic internal variable–strain rate ($\sigma_1 - x - u_d$) surface. Any point on the surface satisfies the consistency condition. Accordingly, the state points inside the surface are in the elastic range. State points above the surface violate the consistency condition, which means an overestimation of the yield stress of the concrete. The calculation results of the $\sigma_1 - x - u_d$ curve indicate that the proposed model incorporates the reduction in stress caused by variations in strain rate during the A_1A_2 stage. The loading–unloading criterion proposed in Section "Flow Rule" can be used to judge whether changes in strain rate cause the plastic flow of concrete materials. For the plastic loading state with a reduced strain rate, u_d is considered as a constitutive variable, so the consistency condition is strictly met throughout the entire loading process. When the yield surface shrinks owing to the reduction of u_d, the stress is simultaneously reduced to ensure that the stress point is always on the yield surface, as shown by the green curve in Fig. 17. u_d is not considered a constitutive variable but rather a constant in the dynamic stress–strain model. This violates the consistency condition when u_d changes during loading. The stress evolves along the curve above the u_d equal to 1 s^{-1} as shown by the blue curve in Fig. 17. This will cause the dynamic stress–strain model to overestimate the concrete strength values, as shown in the curve of the $\sigma_1 - x$ plane in Fig. 17. As a result, the proposed model can be used to forecast the mechanical response of concrete under actual dynamic loading with variable strain rates.

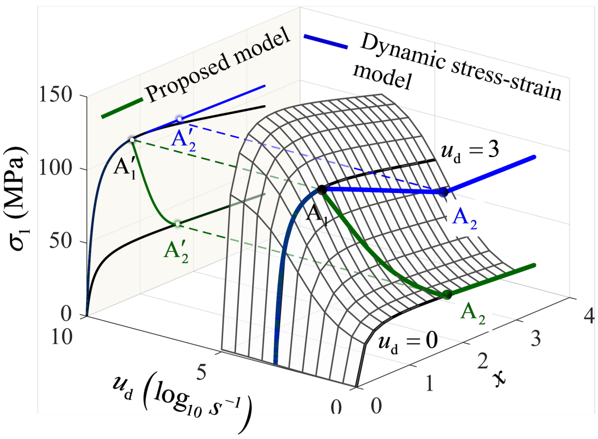

Fig. 17. Comparison of models between stress–strain–strain rate and dynamic stress–strain.

Table 4

The model parameters of concrete under dynamic loading.

Data	E (MPa)	ν	f_c (MPa)	DIF$_{c,max}$	ξ_c	DIF$_{t,max}$	ξ_t	$\varepsilon^p_{1,ds}$	A_1	D	μ
Constant-strain rate	22000	0.2	33.97	1.4	1.4	16	1.4	0.0005	6	0.2	1.9
Yan and Lin (2007)	14000	0.2	9.84	1.38	1.3	16	1.4	0.0004	8	0.8	1.9
Grote et al. (2001)	42500	0.2	46.00	5.60	6.0	16	1.4	0.004	14	1.0	1.0

Variable-strain rate	22000	0.2	33.97	1.42	1.9	16	1.4	0.0005	8	0.4	1.0

Conclusions

The classical stress–strain relationship is developed into a stress–strain–environment relationship by introducing the environmental variables into the yield function as constitutive variables. The established model can describe the mechanical response of materials caused by environmental changes. A loading–unloading criterion was established in the combined coordinate space of the strain and the environmental variable. The state information and load increment of the material could be presented geometrically to evaluate their position relationship with the current yield surface. The conditions under which the material undergoes plastic deformation can be reasonably determined.

Taking the strain rate as an environmental variable, an incremental stress–strain–strain rate relation of concrete is established based on the proposed modeling method. A dynamic closed yield function is proposed that considers strain rate in strength parameters to determine the elastic domain for various rates. The plastic deformation produced by the independent change in strain rate can be captured since strain rate is treated as a constitutive variable when performing consistency conditions. In addition, the corresponding loading/unloading criterion is established to judge the conditions of triggering plastic deformation of concrete materials under the joint drive of strain and strain rate. The model's capability is evaluated under different stress states and strain rate ranges by contrasting model simulations with experimental findings obtained by the author and published papers. In particular, the simulation results for an experiment with a rapidly changing strain rate show that the established model is capable of capturing stress state changes caused by strain rate changes, which is beyond the depth of the dynamic stress–strain model. The good performance of the established model further confirms the feasibility of the proposed modeling method.

Appendix I. DIF

The definition of DIF is the ratio of the dynamic strength to the static strength (Lu et al., 2017) as follows:

$$\mathrm{DIF}_i\left(u_\mathrm{d}\right)=\frac{f_i^\mathrm{d}}{f_i} \tag{24}$$

where the subscript i denotes the state of stress. DIF_i is the dynamic increase factor in different stress states. $u_\mathrm{d}=\lg(\dot{\varepsilon}_\mathrm{d})$. $\dot{\varepsilon}_\mathrm{d}$ is the generalized shear rate expressed by:

$$\dot{\varepsilon}_\mathrm{d}=\sqrt{2/3\left(\dot{\varepsilon}_{ij}-\dot{\varepsilon}_\mathrm{v}\delta_{ij}/3\right)\left(\dot{\varepsilon}_{ij}-\dot{\varepsilon}_\mathrm{v}\delta_{ij}/3\right)} \tag{25}$$

where $\dot{\varepsilon}_\mathrm{v}$ is the volumetric strain rate. Under uniaxial stress conditions, $\dot{\varepsilon}_2=\dot{\varepsilon}_3=-\nu\cdot\dot{\varepsilon}_1$ and $\dot{\varepsilon}_\mathrm{d}$ can be re-expressed in terms of $\dot{\varepsilon}_1$ as:

$$\dot{\varepsilon}_\mathrm{d}=\frac{2}{3}\left(1+\nu\right)\dot{\varepsilon}_1 \tag{26}$$

where ν is Poisson's ratio and it is independent of loading rate (Yan and Lin, 2006). Simultaneous logarithms on both sides of Eq. (26) yield:

$$u_\mathrm{d}=\lg\dot{\varepsilon}_1+\lg\frac{2}{3}\left(1+\nu\right) \tag{27}$$

where u_d acts as an internal variable to drive the evolution of DIF. An S-type (sigmoid) DIF that can consider the ultimate dynamic strength is adopted, as shown in Fig. 18. The dynamic increase factor is expressed as:

$$\mathrm{DIF}_i(u_\mathrm{d})=1+\frac{\mathrm{DIF}_{i,\max}-1}{1+\left[\left(\mathrm{DIF}_{i,\max}-1\right)/\left(\mathrm{DIF}_{i,0}-1\right)-1\right]\exp\left[-\xi_i\left(u_\mathrm{d}-u_{i,\mathrm{d}0}\right)\right]} \tag{28}$$

where $\left(u_{i,\mathrm{d}0},\mathrm{DIF}_{i,0}\right)$ is the reference point. $\mathrm{DIF}_{i,\max}$ and ξ_i represent the material parameters (Lu et al., 2017). $\mathrm{DIF}_{i,\max}$ represents the maximum value of the material's dynamic strength, i.e., $\mathrm{DIF}_{i,\max}=\max(\mathrm{DIF}_i)$. The growth rate of initial strength with strain rate is reflected by ξ_i.

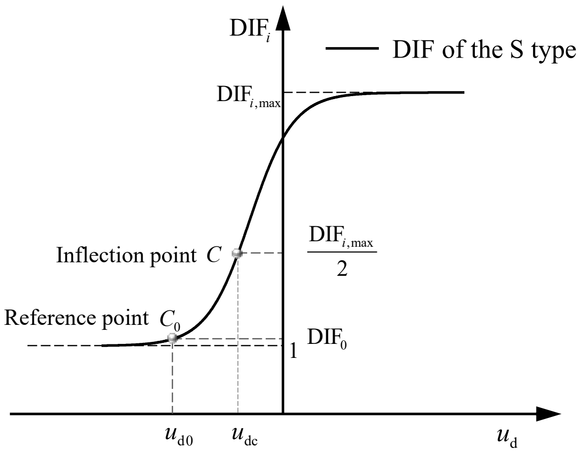

Fig. 18. S-type dynamic increase factor.

Appendix II. Elements required for dynamic constitutive model

The consistency condition of strain rate as a constitutive variable can be expressed:

$$\mathrm{d}f=\left(\frac{\partial f}{\partial \boldsymbol{\sigma}}+\frac{\partial f}{\partial H}\frac{\partial H}{\partial \boldsymbol{\sigma}}\right):\mathrm{d}\boldsymbol{\sigma}+\frac{\partial f}{\partial H}\frac{\partial H}{\partial \boldsymbol{\varepsilon}^{\mathrm{p}}}:\mathrm{d}\boldsymbol{\varepsilon}^{\mathrm{p}}+\frac{\partial f}{\partial u_{\mathrm{d}}}\mathrm{d}u_{\mathrm{d}}=0 \tag{29}$$

Combining Eq. (29) with the derivation process of Section "Modeling Method in the Incremental Stress–Strain–Environment Form" can define $\mathrm{d}\Lambda$ as follows:

$$\mathrm{d}\Lambda=\frac{\left(\dfrac{\partial f}{\partial \boldsymbol{\sigma}}+\dfrac{\partial f}{\partial H}\dfrac{\partial H}{\partial \boldsymbol{\sigma}}\right):\mathbf{D}^{\mathrm{e}}:\mathrm{d}\boldsymbol{\varepsilon}+\dfrac{\partial f}{\partial u_{\mathrm{d}}}\mathrm{d}u_{\mathrm{d}}}{\left(\dfrac{\partial f}{\partial \boldsymbol{\sigma}}+\dfrac{\partial f}{\partial H}\dfrac{\partial H}{\partial \boldsymbol{\sigma}}\right):\mathbf{D}^{\mathrm{e}}:\mathbf{r}-\dfrac{\partial f}{\partial H}\dfrac{\partial H}{\partial \boldsymbol{\varepsilon}^{\mathrm{p}}}:\mathbf{r}} \tag{30}$$

The dynamic constitutive relationship can be established:

$$\mathrm{d}\boldsymbol{\sigma}=\left[\mathbf{D}^{\mathrm{e}}-\frac{\left(\mathbf{D}^{\mathrm{e}}:\mathbf{r}\right)\otimes\left(\dfrac{\partial f}{\partial \boldsymbol{\sigma}}+\dfrac{\partial f}{\partial H}\dfrac{\partial H}{\partial \boldsymbol{\sigma}}\right):\mathbf{D}^{\mathrm{e}}}{\left(\dfrac{\partial f}{\partial \boldsymbol{\sigma}}+\dfrac{\partial f}{\partial H}\dfrac{\partial H}{\partial \boldsymbol{\sigma}}\right):\mathbf{D}^{\mathrm{e}}:\mathbf{r}-\dfrac{\partial f}{\partial H}\dfrac{\partial H}{\partial \boldsymbol{\varepsilon}^{\mathrm{p}}}:\mathbf{r}}\right]:\mathrm{d}\boldsymbol{\varepsilon}-\frac{\left(\mathbf{D}^{\mathrm{e}}:\mathbf{r}\right)\otimes(\dfrac{\partial f}{\partial u_{\mathrm{d}}}\mathrm{d}u_{\mathrm{d}})}{\left(\dfrac{\partial f}{\partial \boldsymbol{\sigma}}+\dfrac{\partial f}{\partial H}\dfrac{\partial H}{\partial \boldsymbol{\sigma}}\right):\mathbf{D}^{\mathrm{e}}:\mathbf{r}-\dfrac{\partial f}{\partial H}\dfrac{\partial H}{\partial \boldsymbol{\varepsilon}^{\mathrm{p}}}:\mathbf{r}} \tag{31}$$

where $\partial f/\partial u_{\mathrm{d}}=\left(\partial f/\partial f_{\mathrm{c}}^{\mathrm{d}}\right)\left(\partial f_{\mathrm{c}}^{\mathrm{d}}/\partial u_{\mathrm{d}}\right)+\left(\partial f/\partial m_0^{\mathrm{d}}\right)\left(\partial m_0^{\mathrm{d}}/\partial u_{\mathrm{d}}\right)$.

The matrix form of the elastic stiffness tensor ($\mathbf{D}^{\mathrm{e}}$) is:

$$\left[\mathbf{D}^{\mathrm{e}}\right]=\frac{E}{(1+\nu)(1-2\nu)}\begin{bmatrix} 1-\nu & \nu & \nu & 0 & 0 & 0 \\ \nu & 1-\nu & \nu & 0 & 0 & 0 \\ \nu & \nu & 1-\nu & 0 & 0 & 0 \\ 0 & 0 & 0 & \frac{1-2\nu}{2} & 0 & 0 \\ 0 & 0 & 0 & 0 & \frac{1-2\nu}{2} & 0 \\ 0 & 0 & 0 & 0 & 0 & \frac{1-2\nu}{2} \end{bmatrix} \tag{32}$$

$\partial f / \partial \boldsymbol{\sigma}$ is also defined as:

$$\frac{\partial f}{\partial \boldsymbol{\sigma}}=\frac{\partial f}{\partial p}\frac{\partial p}{\partial \boldsymbol{\sigma}}+\frac{\partial f}{\partial q}\frac{\partial q}{\partial \boldsymbol{\sigma}}+\frac{\partial f}{\partial r}\frac{\partial r}{\partial \cos\theta}\frac{\partial \cos\theta}{\partial \cos 3\theta}\frac{\partial \cos 3\theta}{\partial \boldsymbol{\sigma}} \tag{33}$$

where

$$\frac{\partial f}{\partial p}=4a_4\cdot p^3+3a_3\cdot p^2+2a_2\cdot p+a_1 \tag{34}$$

where a_i is expressed in Eq. (21).

$$\frac{\partial p}{\partial \sigma_{ij}}=\frac{1}{3}\delta_{ij} \tag{35}$$

in which

$$\begin{Bmatrix} \frac{\partial p}{\partial \sigma_{11}} \\ \frac{\partial p}{\partial \sigma_{22}} \\ \frac{\partial p}{\partial \sigma_{33}} \\ 2\frac{\partial p}{\partial \sigma_{12}} \\ 2\frac{\partial p}{\partial \sigma_{23}} \\ 2\frac{\partial p}{\partial \sigma_{31}} \end{Bmatrix}=\frac{1}{3}\begin{Bmatrix} 1 \\ 1 \\ 1 \\ 0 \\ 0 \\ 0 \end{Bmatrix} \tag{36}$$

$$\frac{\partial f}{\partial q}=4b_4\cdot q^3+3b_3\cdot q^2+2b_2\cdot q+b_1 \tag{37}$$

where b_i is expressed in Eq. (22).

$$\frac{\partial q}{\partial \sigma_{ij}}=\frac{3\left(\sigma_{ij}-p\delta_{ij}\right)}{2q} \tag{38}$$

in which

$$\begin{Bmatrix} \dfrac{\partial q}{\partial \sigma_{11}} \\ \dfrac{\partial q}{\partial \sigma_{22}} \\ \dfrac{\partial q}{\partial \sigma_{33}} \\ 2\dfrac{\partial q}{\partial \sigma_{12}} \\ 2\dfrac{\partial q}{\partial \sigma_{23}} \\ 2\dfrac{\partial q}{\partial \sigma_{31}} \end{Bmatrix} = \frac{3}{2q} \begin{Bmatrix} \sigma_{11} - p \\ \sigma_{22} - p \\ \sigma_{33} - p \\ 2\sigma_{12} \\ 2\sigma_{23} \\ 2\sigma_{31} \end{Bmatrix} \tag{39}$$

$$\frac{\partial f}{\partial r} = \frac{m_0^{\mathrm{d}} H^2 q}{3 f_{\mathrm{c}}^{\mathrm{d}}} \tag{40}$$

$$\frac{\partial\left[r(\cos\theta)\right]}{\partial\cos\theta} = 2\left[r(\cos\theta)\right]\left(1-e^2\right)\frac{\left\{4\cos\theta - \left[r(\cos\theta)\right]\right\}\sqrt{4\left(1-e^2\right)\cos^2\theta + 5e^2 - 4e} - 2\left[r(\cos\theta)\right](2e-1)\cos\theta}{\left[4\left(1-e^2\right)\cos^2\theta + (2e-1)^2\right]\sqrt{4\left(1-e^2\right)\cos^2\theta + 5e^2 - 4e}} \tag{41}$$

$$\frac{\partial \cos\theta}{\partial \cos 3\theta} = \frac{1}{3\left(4\cos^2\theta - 1\right)} \tag{42}$$

$$\frac{\partial \cos 3\theta}{\partial \sigma_{mn}} = \frac{6\sqrt{3} J_2 \left(s_{km} s_{nk} - \dfrac{2}{3} J_2 \delta_{mn}\right) - 9\sqrt{3} J_3 s_{mn}}{4 J_2^{5/2}} \tag{43}$$

in which

$$\begin{Bmatrix} \dfrac{\partial \cos 3\theta}{\partial \sigma_{11}} \\ \dfrac{\partial \cos 3\theta}{\partial \sigma_{22}} \\ \dfrac{\partial \cos 3\theta}{\partial \sigma_{33}} \\ 2\dfrac{\partial \cos 3\theta}{\partial \sigma_{12}} \\ 2\dfrac{\partial \cos 3\theta}{\partial \sigma_{23}} \\ 2\dfrac{\partial \cos 3\theta}{\partial \sigma_{31}} \end{Bmatrix} = \begin{Bmatrix} \dfrac{3\sqrt{3} s_{k1} s_{1k}}{2 J_2^{3/2}} - \dfrac{\sqrt{3}}{J_2^{1/2}} - \dfrac{9\sqrt{3} J_3 s_{11}}{4 J_2^{5/2}} \\ \dfrac{3\sqrt{3} s_{k2} s_{2k}}{2 J_2^{3/2}} - \dfrac{\sqrt{3}}{J_2^{1/2}} - \dfrac{9\sqrt{3} J_3 s_{22}}{4 J_2^{5/2}} \\ \dfrac{3\sqrt{3} s_{k3} s_{3k}}{2 J_2^{3/2}} - \dfrac{\sqrt{3}}{J_2^{1/2}} - \dfrac{9\sqrt{3} J_3 s_{33}}{4 J_2^{5/2}} \\ \dfrac{3\sqrt{3} s_{k1} s_{2k}}{2 J_2^{3/2}} - \dfrac{9\sqrt{3} J_3 s_{12}}{4 J_2^{5/2}} \\ \dfrac{3\sqrt{3} s_{k2} s_{3k}}{2 J_2^{3/2}} - \dfrac{9\sqrt{3} J_3 s_{23}}{4 J_2^{5/2}} \\ \dfrac{3\sqrt{3} s_{k3} s_{1k}}{2 J_2^{3/2}} - \dfrac{9\sqrt{3} J_3 s_{31}}{4 J_2^{5/2}} \end{Bmatrix} (k = 1,2,3) \tag{44}$$

$\partial f / \partial H$ is given:

$$\frac{\partial f}{\partial H} = -2(1-H)\left(\frac{q}{3 f_{\mathrm{c}}^{\mathrm{d}}} - \frac{p}{f_{\mathrm{c}}^{\mathrm{d}}}\right)^4 - \frac{2q}{f_{\mathrm{c}}^{\mathrm{d}}}\left(\frac{q}{3 f_{\mathrm{c}}^{\mathrm{d}}} - \frac{p}{f_{\mathrm{c}}^{\mathrm{d}}}\right)^2 + 2 m_0^{\mathrm{d}} H \left[\frac{q}{3 f_{\mathrm{c}}^{\mathrm{d}}} r(\cos\theta) - \frac{p}{f_{\mathrm{c}}^{\mathrm{d}}}\right] - 2H \tag{45}$$

$\partial H/\partial \boldsymbol{\sigma}$ includes the partial derivative of stress-state-related parameters $\varepsilon_{\mathrm{ds}}^{\mathrm{p}}$ and A with respect to $\boldsymbol{\sigma}$ as follows:

$$\frac{\partial H}{\partial \boldsymbol{\sigma}}=\frac{\partial H}{\partial x}\frac{\partial x}{\partial \varepsilon_{\mathrm{ds}}^{\mathrm{p}}}\frac{\partial \varepsilon_{\mathrm{ds}}^{\mathrm{p}}}{\partial q_{\max}}\frac{\partial q_{\max}}{\partial \boldsymbol{\sigma}}+\frac{\partial H}{\partial A}\frac{\partial A}{\partial q_{\max}}\frac{\partial q_{\max}}{\partial \boldsymbol{\sigma}} \tag{46}$$

The elements required in Eq. (46) are given by:

$$\frac{\partial H}{\partial x}=\frac{\left[2(1-D)-A\right]x^2+2(D-1)x+A}{\left[1+(A-2)x+Dx^2\right]^2} \tag{47}$$

$$\frac{\partial x}{\partial \varepsilon_{\mathrm{ds}}^{\mathrm{p}}}=-\frac{\varepsilon_{\mathrm{d}}^{\mathrm{p}}}{\left(\varepsilon_{\mathrm{ds}}^{\mathrm{p}}\right)^2} \tag{48}$$

$$\frac{\partial \varepsilon_{\mathrm{ds}}^{\mathrm{p}}}{\partial q_{\max}}=\frac{33.81\varepsilon_{1,\mathrm{ds}}^{\mathrm{p}}\cdot\exp\left[\ln(13.70)+2.30-2.30\cdot\left(\frac{q_{\max}}{f_{\mathrm{c}}}\right)\right]}{f_{\mathrm{c}}\left\{1+\exp\left[\ln(13.70)+2.30-2.30\cdot\left(\frac{q_{\max}}{f_{\mathrm{c}}}\right)\right]\right\}^2} \tag{49}$$

$$\frac{\partial H}{\partial A}=\frac{x^3-2x^2+x}{\left[1+(A-2)x+Dx^2\right]^2} \tag{50}$$

$$\frac{\partial A}{\partial q_{\max}}=\frac{8.6136A_1\cdot\exp\left[\ln(2.88)+2.22-2.22\cdot\left(\frac{q_{\max}}{f_{\mathrm{c}}}\right)\right]}{f_{\mathrm{c}}\left\{1+\exp\left[\ln(2.88)+2.22-2.22\cdot\left(\frac{q_{\max}}{f_{\mathrm{c}}}\right)\right]\right\}^2} \tag{51}$$

In this paper, $\varepsilon_{\mathrm{d}}^{\mathrm{p}}=\sqrt{2/3\left(\varepsilon_{ij}^{\mathrm{p}}-\varepsilon_{\mathrm{v}}^{\mathrm{p}}\delta_{ij}/3\right)\left(\varepsilon_{ij}^{\mathrm{p}}-\varepsilon_{\mathrm{v}}^{\mathrm{p}}\delta_{ij}/3\right)}$ is the plastic internal variable, term $\partial H/\partial \boldsymbol{\varepsilon}^{\mathrm{p}}:\mathbf{r}$ in the elastoplastic stiffness matrix can be written as $\left(\partial H/\partial \varepsilon_{\mathrm{d}}^{\mathrm{p}}\right)\left(\partial^{\mu} f/\partial q^{\mu}\right)$, and $\partial^{\mu} f/\partial q^{\mu}$ is defined in Section "Flow Rule". $\partial H/\partial \varepsilon_{\mathrm{d}}^{\mathrm{p}}$ can also be determined by:

$$\frac{\partial H}{\partial \varepsilon_{\mathrm{d}}^{\mathrm{p}}}=\frac{\partial H}{\partial x}\frac{\partial x}{\partial \varepsilon_{\mathrm{d}}^{\mathrm{p}}} \tag{52}$$

where

$$\frac{\partial H}{\partial x}=\frac{\left[2(1-D)-A\right]x^2+2(D-1)x+A}{\left[1+(A-2)x+Dx^2\right]^2} \tag{53}$$

$$\frac{\partial x}{\partial \varepsilon_{\mathrm{d}}^{\mathrm{p}}}=\frac{1}{\varepsilon_{\mathrm{ds}}^{\mathrm{p}}} \tag{54}$$

The derivative of *f* corresponding to u_{d} is defined as:

$$\frac{\partial f}{\partial u_{\mathrm{d}}}=\frac{\partial f}{\partial f_{\mathrm{c}}^{\mathrm{d}}}\frac{\partial f_{\mathrm{c}}^{\mathrm{d}}}{\partial u_{\mathrm{d}}}+\frac{\partial f}{\partial m_{0}^{\mathrm{d}}}\frac{\partial m_{0}^{\mathrm{d}}}{\partial u_{\mathrm{d}}} \tag{55}$$

where

$$\frac{\partial f}{\partial f_{\mathrm{c}}^{\mathrm{d}}}=-12(1-H)^{2}(q-3p)^{4}\left(3f_{\mathrm{c}}^{\mathrm{d}}\right)^{-5}-\frac{2}{3}q(1-H)(q-3p)^{2}\left(f_{\mathrm{c}}^{\mathrm{d}}\right)^{-4}-2q^{2}\left(f_{\mathrm{c}}^{\mathrm{d}}\right)^{-3}-\frac{1}{3}m_{0}^{\mathrm{d}}H^{2}\left[qr(\cos\theta)-3p\right]\left(f_{\mathrm{c}}^{\mathrm{d}}\right)^{-2} \tag{56}$$

$$\frac{\partial f_{\mathrm{c}}^{\mathrm{d}}}{\partial u_{\mathrm{d}}}=\frac{\left(\mathrm{DIF}_{\mathrm{c,max}}-1\right)\cdot\xi_{\mathrm{c}}\cdot\left\{\left[\left(\mathrm{DIF}_{\mathrm{c,max}}-1\right)/\left(\mathrm{DIF}_{0}-1\right)-1\right]\exp\left[-\xi_{\mathrm{c}}\left(u_{\mathrm{d}}-u_{0}\right)\right]\right\}\cdot f_{\mathrm{c}}}{\left\{1+\left[\left(\mathrm{DIF}_{\mathrm{c,max}}-1\right)/\left(\mathrm{DIF}_{0}-1\right)-1\right]\exp\left[-\xi_{\mathrm{c}}\left(u_{\mathrm{d}}-u_{0}\right)\right]\right\}^{2}} \tag{57}$$

$$\frac{\partial f}{\partial m_{0}^{\mathrm{d}}}=H^{2}\left[\frac{q}{3f_{\mathrm{c}}^{\mathrm{d}}}r(\cos\theta)-\frac{p}{f_{\mathrm{c}}^{\mathrm{d}}}\right] \tag{58}$$

The strength parameter m_0^{d} comprises $f_{\mathrm{c}}^{\mathrm{d}}$ and $f_{\mathrm{t}}^{\mathrm{d}}$, so the derivative of $f_{\mathrm{c}}^{\mathrm{d}}$ and $f_{\mathrm{t}}^{\mathrm{d}}$ with respect to u_{d} is separately calculated as follows:

$$\frac{\partial m_{0}^{\mathrm{d}}}{\partial u_{\mathrm{d}}}=\frac{\partial m_{0}^{\mathrm{d}}}{\partial f_{\mathrm{c}}^{\mathrm{d}}}\frac{\partial f_{\mathrm{c}}^{\mathrm{d}}}{\partial u_{\mathrm{d}}}+\frac{\partial m_{0}^{\mathrm{d}}}{\partial f_{\mathrm{t}}^{\mathrm{d}}}\frac{\partial f_{\mathrm{t}}^{\mathrm{d}}}{\partial u_{\mathrm{d}}} \tag{59}$$

$$\frac{\partial m_{0}^{\mathrm{d}}}{\partial f_{\mathrm{c}}^{\mathrm{d}}}=\frac{1}{f_{\mathrm{t}}^{\mathrm{d}}}+\frac{f_{\mathrm{t}}^{\mathrm{d}}}{\left(f_{\mathrm{c}}^{\mathrm{d}}\right)^{2}} \tag{60}$$

$$\frac{\partial m_{0}^{\mathrm{d}}}{\partial f_{\mathrm{t}}^{\mathrm{d}}}=-\frac{f_{\mathrm{c}}^{\mathrm{d}}}{\left(f_{\mathrm{t}}^{\mathrm{d}}\right)^{2}}-\frac{1}{f_{\mathrm{c}}^{\mathrm{d}}} \tag{61}$$

$$\frac{\partial f_{\mathrm{t}}^{\mathrm{d}}}{\partial u_{\mathrm{d}}}=\frac{\left(\mathrm{DIF}_{\mathrm{t,max}}-1\right)\cdot\xi_{\mathrm{t}}\cdot\left\{\left[\left(\mathrm{DIF}_{\mathrm{t,max}}-1\right)/\left(\mathrm{DIF}_{0}-1\right)-1\right]\exp\left[-\xi_{\mathrm{t}}\left(u_{\mathrm{d}}-u_{0}\right)\right]\right\}\cdot f_{\mathrm{t}}}{\left\{1+\left[\left(\mathrm{DIF}_{\mathrm{t,max}}-1\right)/\left(\mathrm{DIF}_{0}-1\right)-1\right]\exp\left[-\xi_{\mathrm{t}}\left(u_{\mathrm{d}}-u_{0}\right)\right]\right\}^{2}} \tag{62}$$

Appendix III. Test results at constant-strain rates

We label the specimens U-V-W according to the confining pressure σ_3 and loading rate of the tests to facilitate the display of the test results. U represents the value of σ_3, including 0, 10, and 20 MPa. V equals 1, 2, 3, and 4, indicating $\dot{\varepsilon}_1$ of 10^{-5}, 10^{-4}, 10^{-3}, and 10^{-2} s^{-1} respectively. The test is repeated three times under the same loading condition, and W denotes the test sequence. For example, "0-2-1" represents the first set of tests with $\sigma_3=0\ \mathrm{MPa}$ and $\dot{\varepsilon}_1=10^{-4}\,\mathrm{s}^{-1}$. The test under the same loading condition is repeated three times. The test results of all specimens are summarized in Table 5.

Table 5

Summary of the test results at constant-strain rates.

Specimen Group	Specimen ID	H × D (mm × mm)	$\dot{\varepsilon}_1$ (s^{-1})	$\sigma_1^{peak} - \sigma_3^{peak}$ (MPa)	ε_1^{peak} (%)	ε_3^{peak} (%)	Average $\sigma_1^{peak} - \sigma_3^{peak}$ (MPa)
	0-1-1	199.92 × 99.03	10^{-5}	38.20	0.3409	−0.0841	
0-1	0-1-2	200.38 × 99.04	10^{-5}	33.40	0.2433	−0.2102	35.19
	0-1-3	200.60 × 99.02	10^{-5}	33.97	0.2377	−0.0814	
	0-2-1	199.73 × 98.53	10^{-4}	41.22	0.2044	−0.1266	
0-2	0-2-2	199.72 × 99.01	10^{-4}	38.89	0.3282	−0.0624	39.51
	0-2-3	199.58 × 99.07	10^{-4}	38.41	0.2059	−0.0804	
	0-3-1	199.45 × 99.10	10^{-3}	45.59	0.2424	−0.0933	
0-3	0-3-2	201.40 × 98.92	10^{-3}	47.86	0.2175	−0.0917	45.49
	0-3-3	200.08 × 99.07	10^{-3}	43.02	0.3421	−0.0645	
	0-4-1	200.23 × 98..89	10^{-2}	53.68	0.2231	−0.0933	
0-4	0-4-2	199.73 × 98.92	10^{-2}	49.11	0.2700	−0.0917	49.63
	0-4-3	198.87 × 99.09	10^{-2}	46.09	0.2201	−0.0645	
	10-1-1	199.33 × 99.06	—	—	—	—	
10-1	10-1-2	200.01 × 98.92	10^{-5}	75.35	0.8478	−0.2981	76.87
	10-1-3	201.41 × 99.15	10^{-5}	78.40	0.931	−0.5217	
	10-2-1	200.26 × 99.09	10^{-4}	84.13	0.7020	−0.3157	
10-2	10-2-2	200.48 × 99.08	10^{-4}	88.84	0.6936	−0.2516	86.48
	10-2-3	201.68 × 99.04	—	—	—	—	
	10-3-1	199.85 × 99.03	10^{-3}	92.21	0.6932	−0.2946	
10-3	10-3-2	201.05 × 99.14	10^{-3}	89.06	0.7244	−0.3000	90.67
	10-3-3	199.51 × 99.11	10^{-3}	90.75	0.6586	−0.3086	
	10-4-1	200.84 × 98.98	10^{-2}	92.94	0.8260	−0.2713	
10-4	10-4-2	200.26 × 99.06	10^{-2}	91.01	0.6871	−0.2603	92.59
	10-4-3	201.90 × 99.14	10^{-2}	93.81	0.6441	−0.3398	
	20-1-1	199.31 × 99.12	—	—	—	—	
20-1	20-1-2	200.05 × 99.02	10^{-5}	106.66	1.0632	−0.2206	105.08
	20-1-3	200.13 × 99.10	10^{-5}	103.50	0.9100	−0.2174	
	20-2-1	198.41 × 99.09	10^{-4}	109.77	1.6461	−0.7177	
20-2	20-2-2	200.99 × 99.06	10^{-4}	109.65	1.5179	−0.8186	108.65
	20-2-3	200.36 × 99.06	10^{-4}	106.53	1.2134	−0.4507	
	20-3-1	199.07 × 99.09	10^{-3}	110.21	1.1565	−0.2830	
20-3	20-3-2	200.71 × 99.17	10^{-3}	113.10	0.8787	−0.2165	111.01
	20-3-3	199.03 × 99.11	10^{-3}	109.71	0.9685	−0.2037	
	20-4-1	201.52 × 99.12	—	—	—	—	
20-4	20-4-2	200.08 × 99.19	10^{-2}	119.58	1.0216	−0.3861	118.9
	20-4-3	198.93 × 99.14	10^{-2}	118.39	0.9153	−0.3178	

Note: — means no valid data has been collected

Data Availability Statement

All data, models, or codes that support the findings of this study are available from the corresponding author upon reasonable request.

Acknowledgments

This work was sponsored by the National Natural Science Foundation of China (Grant No. 52025084) and Postdoctoral Research Foundation of China (Grant No. 2022M721884).

Notation

$\boldsymbol{\sigma}$, $\boldsymbol{\varepsilon}$, $\boldsymbol{\varepsilon}^{\mathrm{e}}$, and $\boldsymbol{\varepsilon}^{\mathrm{p}}$	The stress tensor, total strain tensor, elastic strain tensor, and plastic strain tensor
p and θ	The hydrostatic pressure and the stress Lode angle
q and $q_{\max}$	The generalized shear stress and the largest q in the loading history
f_{c} and $f_{\mathrm{c}}^{\mathrm{d}}$	The uniaxial compressive strength and dynamic f_{c}
f_{t} and $f_{\mathrm{t}}^{\mathrm{d}}$	The uniaxial tensile strength and dynamic f_{t}
$f_{\mathrm{bc}}^{\mathrm{d}}$	The dynamic equibiaxial compressive strength
m_0^{d} and e^{d}	The dynamic friction parameter and the dynamic eccentricity parameter
$\varepsilon_{\mathrm{d}}^{\mathrm{p}}$ and $\varepsilon_{\mathrm{v}}^{\mathrm{p}}$	The equivalent plastic shear strain and the plastic volume strain
$\varepsilon_{\mathrm{ds}}^{\mathrm{p}}$ and $\varepsilon_{1,\mathrm{ds}}^{\mathrm{p}}$	$\varepsilon_{\mathrm{d}}^{\mathrm{p}}$ at the peak strength and $\varepsilon_{\mathrm{d}}^{\mathrm{p}}$ at f_{c}
$\dot{\varepsilon}_{\mathrm{d}}$ and $\dot{\varepsilon}_{\mathrm{v}}$	The equivalent shear strain rate and the volume strain rate
x	The ratio of $\varepsilon_{\mathrm{d}}^{\mathrm{p}}$ to $\varepsilon_{\mathrm{ds}}^{\mathrm{p}}$
u_{d}	The logarithm of $\dot{\varepsilon}_{\mathrm{d}}^{\mathrm{p}}$, i.e., $u_{\mathrm{d}}=\log(\dot{\varepsilon}_{\mathrm{d}}^{\mathrm{p}})$
$\mathbf{D}^{\mathrm{e}}$	The elastic stiffness tensor
ψ	The environmental variable
$\mathrm{d}\Lambda$	The plastic multiplier
$\mathbf{r}$ and μ	The plastic flow direction and the fractional order
DIF_i	The dynamic increase factor in different stress states
$\mathrm{DIF}_{i,\max}$ and ξ_i	The maximum value of DIF_i and the growth rate of the initial strength with the strain rate
H	The hardening–softening parameter
A and D	The parameters of H
A_1	A under the uniaxial compression condition
$\boldsymbol{\delta}$	Kronecker delta

Reference

Aráoz, G., B. Luccioni. 2015. “Modeling concrete like materials under sever dynamic pressures.” *Int. J. Impact Eng.* 76: 139-154. https://doi.org/10.1016/j.ijimpeng.2014.09.009.

Bai, Z., Y. X. Liu, J. T. Yang, et al. 2020. “A constitutive model for concrete subjected to extreme dynamic loadings.” *Int. J. Impact Eng.* 138: 103483. https://doi.org/10.1016/j.ijimpeng.2019.103483.

Borrvall, T., W. Riedel. 2011."The RHT concrete model in LS-DYNA". In *Proc., 8th European LS-DYNA Users Conf.*, Strasbourg, France: The Alyotech group.

Candappa, D. C., J. G. Sanjayan, S. Setunge. 2001. “Complete triaxial stress-strain curves of high-strength concrete.” *J. Mater. Civ. Eng.* 13(3): 209-215. https://doi.org/10.1061/(ASCE)0899-1561(2001)13:3(209).

Chang, Y. F., Y. H. Chen, M. S. Sheu, et al. 2006. “Residual stress – strain relationship for concrete after exposure to high temperatures.” *Cem. Concr. Res.* 36(10): 1999-2005. https://doi.org/10.1016/j.cemconres.2006.05.029.

Chen, L., Q. Fang, X. Q. Jiang, et al. 2015. “Combined effects of high temperature and high strain rate on normal weight concrete.” *Int. J. Impact Eng.* 86: 40-56. https://doi.org/10.1016/j.ijimpeng.2015.07.002.

Drucker, D. C. 1950. “Some implications of work hardening and ideal plasticity.” *Q. Appl. Math.* 7(4): 411-418.

Etse, G., K. Willam. 1994. “Fracture energy formulation for inelastic behavior of plain concrete.” *J. Eng. Mech.* 120(9): 1983-2011. https://doi.org/10.1061/(ASCE)0733-9399(1994)120:9(1983).

Fan, Y., L. Chen, R. Q. Yu, et al. 2022. “Experimental study of damage to ultra-high performance concrete slabs subjected to partially embedded cylindrical explosive charges.” *Int. J. Impact Eng.* 168: 104298. https://doi.org/10.1016/j.ijimpeng.2022.104298.

Gao, Z. W., J. D. Zhao. 2017. “A non-coaxial critical-state model for sand accounting for fabric anisotropy and fabric evolution.” *Int. J. Solids Struct.* 106-107: 200-212. https://doi.org/10.1016/j.ijsolstr.2016.11.019.

Gasch, T., R. Malm, A. Ansell. 2016. “A coupled hygro-thermo-mechanical model for concrete subjected to variable environmental conditions.” *Int. J. Solids Struct.* 91: 143-156. https://doi.org/10.1016/j.ijsolstr.2016.03.004.

Gebbeken, N., T. Krauthammer. 2013. "Understanding the dynamic response of concrete to loading: practical examples". In *Understanding the Tensile Properties of Concrete*, 338-369. Cambridge, UK: Woodhead Publishing.

Grassl, P., M. Jirásek. 2006. “Damage-plastic model for concrete failure.” *Int. J. Solids Struct.* 43(22-23): 7166-7196. https://doi.org/10.1016/j.ijsolstr.2006.06.032.

Grote, D. L., S. W. Park, M. Zhou. 2001. “Dynamic behavior of concrete at high strain rates and pressures: I. experimental characterization.” *Int. J. Impact Eng.* 25(9): 869-886. https://doi.org/10.1016/S0734-743X(01)00020-3.

He, Z. J., Y. N. Ma, Z. W. Wang, et al. 2021. “Triaxial strength and deformation characteristics and its constitutive model of high-strength concrete before and after high temperatures.” *Structures* 30: 1127-1138. https://doi.org/10.1016/j.istruc.2020.11.078.

Heeres, O. M., A. S. J. Suiker, R. de Borst. 2002. “A comparison between the Perzyna viscoplastic model and the Consistency viscoplastic model.” *Eur. J. Mech. A-Solids* 21(1): 1-12. https://doi.org/10.1016/S0997-7538(01)01188-3.

Holmquist, T. J., G. R. Johnson. 2011. “A computational constitutive model for glass subjected to large strains, high strain rates and high pressures.” *J. Appl. Mech.* 78(5). https://doi.org/10.1115/1.4004326.

Hossain, A. B., J. Weiss. 2004. “Assessing residual stress development and stress relaxation in restrained concrete ring specimens.” *Cem. Concr. Compos.* 26(5): 531-540. https://doi.org/10.1016/S0958-9465(03)00069-6.

Il'Iushin, A. A. 1961. “On the postulate of plasticity.” *J. Appl. Math. Mech.* 25(3): 746-752.

https://doi.org/10.1016/0021-8928(61)90044-2.

Imran, I., S. J. Pantazopoulou. 1996. “Experimental study of plain concrete under triaxial stress.” *ACI Mater. J.* 93(6): 589-601. https://doi.org/10.14359/9865.

Jia, P. C., H. Wu, Q. Fang. 2023. “An improved 2DOF model for dynamic behaviors of RC members under lateral low-velocity impact.” *Int. J. Impact Eng.* 173: 104460. https://doi.org/10.1016/j.ijimpeng.2022.104460.

Kang, H. D., K. J. Willam. 2000. “Performance evaluation of elastoviscoplastic concrete model.” *J. Eng. Mech.* 126(9): 995-1000. https://doi.org/10.1061/(ASCE)0733-9399(2000)126:9(995).

Khan, A. S., H. Liu. 2012. “Variable strain rate sensitivity in an aluminum alloy: Response and constitutive modeling.” *Int. J. Plast.* 36: 1-14. https://doi.org/10.1016/j.ijplas.2012.02.001.

Kong, X. Z., Q. Fang, L. Chen, et al. 2018. “A new material model for concrete subjected to intense dynamic loadings.” *Int. J. Impact Eng.* 120: 60-78. https://doi.org/10.1016/j.ijimpeng.2018.05.006.

Kong, X. Z., Q. Fang, Q. M. Li, et al. 2017. “Modified K&C model for cratering and scabbing of concrete slabs under projectile impact.” *Int. J. Impact Eng.* 108: 217-228. https://doi.org/10.1016/j.ijimpeng.2017.02.016.

Kupfer, H., H. K. Hilsdorf, H. Rusch. 1969. “Behavior of concrete under biaxial stresses.” *J. Proc.* 66(8). https://doi.org/10.14359/7388.

Li, Q. M., Y. B. Lu, H. Meng. 2009. “Further investigation on the dynamic compressive strength enhancement of concrete-like materials based on split Hopkinson pressure bar tests. Part II: Numerical simulations.” *Int. J. Impact Eng.* 36(12): 1335-1345. https://doi.org/10.1016/j.ijimpeng.2009.04.010.

Lu, D. C., X. Zhou, X. L. Du, et al. 2020. “3D dynamic elastoplastic constitutive model of concrete within the framework of rate-dependent consistency condition.” *J. Eng. Mech.* 146(11): 4020124. https://doi.org/10.1061/(ASCE)EM.1943-7889.0001854.

Lu, D. C., C. C. Su, X. Zhou, et al. 2022. “A cohesion-friction combined hardening plastic model of concrete with the nonorthogonal flow rule: Theory and numerical implementation." *Constr. Build. Mater.* 325: 126586. https://doi.org/10.1016/j.conbuildmat.2022.126586.

Lu, D. C., X. Zhou, X. L. Du, et al. 2019. "A 3D fractional elastoplastic constitutive model for concrete material." *Int. J. Solids Struct.* 165: 160-175. https://doi.org/10.1016/j.ijsolstr.2019.02.004.

Lu, D. C., F. P. Meng, X. Zhou, et al. 2022. "Double scalar variables plastic-damage model for concrete." *J. Eng. Mech.* 148(2): 4021143. https://doi.org/10.1061/(ASCE)EM.1943-7889.0002050.

Lu, D. C., G. S. Wang, X. L. Du, et al. 2017. "A nonlinear dynamic uniaxial strength criterion that considers the ultimate dynamic strength of concrete." *Int. J. Impact Eng.* 103: 124-137. https://doi.org/10.1016/j.ijimpeng.2017.01.011.

Lu, X. B., C. T. Hsu. 2007. "Stress-strain relations of high-strength concrete under triaxial compression." *J. Mater. Civ. Eng.* 19(3): 261-268. https://doi.org/10.1061/(ASCE)0899-1561(2007)19:3(261).

Lucchesi, M., P. Podio-Guidugli. 1995. "Elastic unloading, neutral loading, and plastic loading in the theory of materials with elastic range." *Int. J. Plast.* 11(1): 1-14. https://doi.org/10.1016/0749-6419(94)00036-0.

Ma, J. J., J. J. Chen, W. X. Chen, et al. 2022. "A coupled thermal-elastic-plastic-damage model for concrete subjected to dynamic loading." *Int. J. Plast.* 153: 103279. https://doi.org/10.1016/j.ijplas.2022.103279.

Malvar, L. J., J. E. Crawford, J. W. Wesevich, et al. 1997. "A plasticity concrete material model for DYNA3D." *Int. J. Impact Eng.* 19(9): 847-873. https://doi.org/10.1016/S0734-743X(97)00023-7.

Naghdi, P. M., S. A. Murch. 1963. "On the mechanical behavior of viscoelastic/plastic solids." *J. Appl. Mech.* 30(3): 321-328. https://doi.org/10.1115/1.3636556.

Paliwal, B., Y. Hammi, M. Chandler, et al. 2020. "A three-invariant cap-viscoplastic rate-dependent-damage model for cementitious materials with return mapping integration in Haigh-Westergaard coordinate space." *Int. J. Solids Struct.* 182-183: 77-99. https://doi.org/10.1016/j.ijsolstr.2019.07.029.

Peng, Q., H. Wu, P. C. Jia, et al. 2023. "Dynamic behavior of UHPC member under lateral low-velocity impact: Mesoscale analysis." *Int. J. Impact Eng.* 172: 104418. https://doi.org/10.1016/j.ijimpeng.2022.104418.

Polanco-Loria, M., O. S. Hopperstad, T. Børvik, et al. 2008. "Numerical predictions of ballistic limits for concrete slabs using a modified version of the HJC concrete model." *Int. J. Impact Eng.* 35(5): 290-303. https://doi.org/10.1016/j.ijimpeng.2007.03.001.

Qi, C. Z., M. Y. Wang, Q. H. Qian. 2009. "Strain-rate effects on the strength and fragmentation size of rocks." *Int. J. Impact Eng.* 36(12): 1355-1364. https://doi.org/10.1016/j.ijimpeng.2009.04.008.

Qiao, Y. F., A. Ferrari, L. Laloui, et al. 2016. "Nonstationary flow surface theory for modeling the viscoplastic behaviors of soils." *Comput. Geotech.* 76: 105-119. https://doi.org/10.1016/j.compgeo.2016.02.015.

Rahnavard, R., H. D. Craveiro, R. A. Simões, et al. 2022. "Fire resistance of concrete-filled cold-formed steel (CF-CFS) built-up short columns." *J. Build. Eng.* 48: 103854. https://doi.org/10.1016/j.jobe.2021.103854.

Reis, J. M. L., L. J. Pacheco, H. S. Da Costa Mattos. 2014. "Temperature and variable strain rate sensitivity in recycled HDPE." *Polym. Test* 39: 30-35. https://doi.org/10.1016/j.polymertesting.2014.07.011.

Shkolnik, I. E. 2008. "Influence of high strain rates on stress – strain relationship, strength and elastic modulus of concrete." *Cem. Concr. Compos.* 30(10): 1000-1012. https://doi.org/10.1016/j.cemconcomp.2007.10.001.

Torelli, G., P. Mandal, M. Gillie, et al. 2018. "A confinement-dependent load-induced thermal strain constitutive model for concrete subjected to temperatures up to 500 °C." *Int. J. Mech. Sci.* 144: 887-896. https://doi.org/10.1016/j.ijmecsci.2017.12.054.

Wang, G. S., D. C. Lu, X. L. Du, et al. 2018. "Dynamic multiaxial strength criterion for concrete based on strain rate – dependent strength parameters." *J. Eng. Mech.* 144(5): 4018018. https://doi.org/10.1061/(ASCE)EM.1943-7889.0001428.

Wang, G. S., D. C. Lu, X. L. Du, et al. 2018. "A true 3D frictional hardening elastoplastic constitutive model of concrete based on a unified hardening/softening function.” *J. Mech. Phys. Solids* 119: 250-273. https://doi.org/10.1016/j.jmps.2018.06.019.

Wehner, M., S. I. Seneviratne, X. Zhang, et al. 2021."Weather and Climate Extreme Events in a Changing Climate. ". In *AGU Fall Meeting* 2021, New Orleans, United States: Intergovernmental Panel on Climate Change.

Wu, H., Q. Fang, Y. Peng, et al. 2015. “Hard projectile perforation on the monolithic and segmented RC panels with a rear steel liner.” *Int. J. Impact Eng.* 76: 232-250. https://doi.org/10.1016/j.ijimpeng.2014.10.010.

Yan, D., G. Lin. 2007. “Dynamic behaviour of concrete in biaxial compression.” *Mag. Concr. Res.* 59(1): 45-52. https://doi.org/10.1680/macr.2007.59.1.45.

Yan, D. M., G. Lin. 2006. “Dynamic properties of concrete in direct tension.” *Cem. Concr. Res.* 36(7): 1371-1378. https://doi.org/10.1016/j.cemconres.2006.03.003.

Yu, S. S., Y. B. Lu, Y. Cai. 2013. “The strain-rate effect of engineering materials and its unified model.” *Lat. Am. J. Solids Struct.* 10: 833-844. https://doi.org/10.1590/S1679-78252013000400010.

Zeng, Y. Q., L. H. Xu, Y. Chi, et al. 2023. “Compressive behavior of circular GFRP tube-confined UHPC-filled steel-encased stub columns.” *Compos. Struct.* 309: 116730. https://doi.org/10.1016/j.compstruct.2023.116730.

Zhang, Q. B., J. Zhao. 2014. “A review of dynamic experimental techniques and mechanical behaviour of rock materials.” *Rock Mech. Rock Eng.* 47(4): 1411-1478. https://doi.org/10.1007/s00603-013-0463-y.

Zheng, B. T., J. G. Teng. 2022. “A plasticity constitutive model for concrete under multiaxial compression.” *Eng. Struct.* 251: 113435. https://doi.org/10.1016/j.engstruct.2021.113435.

Zhou, X., D. C. Lu, X. L. Du, et al. 2020. “A 3D non-orthogonal plastic damage model for concrete.” *Comput. Meth. Appl. Mech. Eng.* 360: 112716. https://doi.org/10.1016/j.cma.2019.112716.